AWARD NUMBER: W81XWH-14-1-0024

TITLE: Photoacoustic and Ultrasonic Image-Guided Needle Biopsy of the Prostate

PRINCIPAL INVESTIGATOR: Richard Bouchard

CONTRACTING ORGANIZATION: University of Texas MD Anderson Cancer Center
Houston, TX 77030

REPORT DATE: October 2015

TYPE OF REPORT: Final

PREPARED FOR: U.S. Army Medical Research and Materiel Command
Fort Detrick, Maryland 21702-5012

REPORT DOCUMENTATION PAGE			*Form Approved* OMB No. 0704-0188
Public reporting burden for this collection of information is estimated to average 1 hour per response, including the time for reviewing instructions, searching existing data sources, gathering and maintaining the data needed, and completing and reviewing this collection of information. Send comments regarding this burden estimate or any other aspect of this collection of information, including suggestions for reducing this burden to Department of Defense, Washington Headquarters Services, Directorate for Information Operations and Reports (0704-0188), 1215 Jefferson Davis Highway, Suite 1204, Arlington, VA 22202-4302. Respondents should be aware that notwithstanding any other provision of law, no person shall be subject to any penalty for failing to comply with a collection of information if it does not display a currently valid OMB control number. **PLEASE DO NOT RETURN YOUR FORM TO THE ABOVE ADDRESS.**

1. REPORT DATE	2. REPORT TYPE	3. DATES COVERED
October 2015	Final	1 Feb 2014 - 31 Jul 2015

4. TITLE AND SUBTITLE

Photoacoustic and Ultrasonic Image-Guided Needle Biopsy of the Prostate

5a. CONTRACT NUMBER
W81XWH-14-1-0024

5b. GRANT NUMBER
W81XWH-14-1-0024

5c. PROGRAM ELEMENT NUMBER

6. AUTHOR(S) Richard Bouchard, David Fuentes, John Ward, Trevor Mitcham, Houra Taghavi

5d. PROJECT NUMBER

5e. TASK NUMBER

5f. WORK UNIT NUMBER

E-Mail: rrbouchard@mdanderson.org

7. PERFORMING ORGANIZATION NAME(S) AND ADDRESS(ES)
University of Texas MD Anderson
Thomas E. Wilson
1515 Holcombe Blvd Unit 207
Houston, TX 77030

8. PERFORMING ORGANIZATION REPORT NUMBER

9. SPONSORING / MONITORING AGENCY NAME(S) AND ADDRESS(ES)

U.S. Army Medical Research and Materiel Command

Fort Detrick, Maryland 21702-5012

10. SPONSOR/MONITOR'S ACRONYM(S)

11. SPONSOR/MONITOR'S REPORT NUMBER(S)

12. DISTRIBUTION / AVAILABILITY STATEMENT

Approved for Public Release; Distribution Unlimited

13. SUPPLEMENTARY NOTES

14. ABSTRACT

We have optimized interstitial light sources to yield multi-spectral photoacoustic (PA) imaging data in excised prostate tissue. Two types of interstitial sources — a directional source and an omnidirectional source — have been optimized and validated in gelatin (tissue-mimicking) and tissue phantoms with exogenous and endogenous contrast. Imaging with an external linear and transrectal array has been demonstrated in real-time at tissue depths in excess of 7 cm and with improved spectral fidelity (i.e., reduced redshift in obtained spectra) using the Verasonics ultrasound platform, is suited for eventual clinical trials. The Verasonics acquisition is performed in a Delrin holder and coordinated with a LabVIEW data acquisition device to allow for energy correction and eventual 3D spatial registration. Model-based reconstruction of the oxygen saturation distribution (and underlying fluence and PA pressure distributions) has been developed. This preliminary work has laid the foundation for prostate biopsies augmented with interstitially driven PA imaging.

15. SUBJECT TERMS
photoacoutic imaging; prostate biopsy; interstitial irradiation; oxygen saturation estimation; model-based reconstruction

16. SECURITY CLASSIFICATION OF:			17. LIMITATION OF ABSTRACT	18. NUMBER OF PAGES	19a. NAME OF RESPONSIBLE PERSON USAMRMC
a. REPORT Unclassified	**b. ABSTRACT** Unclassified	**c. THIS PAGE** Unclassified	Unclassified	34	19b. TELEPHONE NUMBER *(include area code)*

Standard Form 298 (Rev. 8-98)
Prescribed by ANSI Std. Z39.18

Table of Contents

1. Introduction: Needle biopsy, the standard of care for prostate cancer diagnosis, requires sampling of predetermined regions of the prostate to systematically spread coverage throughout the gland. Because the clinician typically performs this procedure blind of a gland's specific pathology (e.g., lesions not apparent under transrectal ultrasound [TRUS]), however, conventional biopsy schemes have relatively high false-negative rates or sample an increasingly greater number of biopsy cores (e.g., saturation techniques). The necessity for follow-up biopsies delays treatment, while increasing the number of biopsy cores increases the risk of complications, including hematuria and rectal bleeding. To improve the sensitivity of needle biopsy procedures, the research proposed herein offers an adaptive biopsy needle placement paradigm that is guided by TRUS and PA imaging techniques. PA imaging uses non-damaging, pulsed laser irradiation to transform chromophores (e.g., hemoglobin) in tissue into acoustic sources through the processes of optical absorption and thermoelastic expansion. These acoustic transmissions, which permit deeper (i.e., cm-order) interrogations than typical optical techniques, can then be imaged with conventional ultrasound arrays, providing a map of tissue constituents' optical absorption spectra. Due to its spectroscopic capabilities, PA imaging is able to probe the oxygen saturation of tissue and assess local hypoxia, which has been shown to correlate with the presence/aggressiveness of prostate carcinomas. This study uses an optical fiber to assess local hypoxia within a needle tract with PA imaging. Such a design allows for local irradiation and permits deeper interrogation depths. Local light delivery should provide a sufficient SNR to assess the oxygenation state of endogenous hemoglobin in a radius (<1 cm) about the needle. These data will allow for the estimation of a tissue hypoxia map, which will drive an adaptive needle placement algorithm that provides the clinician with intraoperative, real-time indications of "suspicious" regions in the prostate that should be targeted for biopsy.

2. Keywords: photoacoutic imaging; prostate biopsy; interstitial irradiation; oxygen saturation estimation; model-based reconstruction

3. Accomplishments

Major Goals:

The following milestones were established for the project's statement of work:

a) Physical PA-needle prototype with holder will be constructed and integrated into LabVIEW. (3 months) – PA-needle prototypes completed ~5 months; LabVIEW integration achieved ~12 months; holder construction/integration achieved ~15 months.

b) PA-needle imaging data and position data will be integrated into a MATLAB-based interface to provide adaptive likelihood maps. (5 months) – actual completion ~12 months.

c) A tissue-mimicking phantom compatible with the PA-needle system will be constructed and ready for use. (7 months) – actual completion ~3 months.

d) A working PA-needle prototype will be constructed, and its imaging parameters will be characterized. (12 months) – actual completion ~6 months.

Accomplishments:

1) Major Activities and Specific Objectives
a) Development and utilization of an interstitially-driven PA imaging system with real-time visualization.
b) Integration of a transrectal probe for PA imaging of the prostate.
c) Development and utilization of a tissue-mimicking phantom for PA prostate imaging.
d) Development of a model-based reconstruction platform for oxygen saturation estimation in the prostate.
e) Integration of imaging system information (e.g., pulse energy) into a LabVIEW data acquisition and control environment.
f) Construction of biocompatible Delrin holder for precision probe positioning.

2) Significant Results
We have successfully achieved real-time PA imaging of prostate and liver tissue with two different types of interstitial irradiation; this work has been included in greater detail in the attached peer-reviewed publication. PA imaging is generally implemented with external irradiation, but we have shown that local irradiation provides a better signal-to-noise ratio (SNR) at depths away from the US transducer and yields improved spectral fidelity to characterize absorbers (due to reduced optical-scattering distances). As part of this work, we developed and optimized two different optical fibers: a side-fire fiber (Fig. 1.a,c) and a conical-tip fiber (Fig. 1.b,d). The side-fire fiber was able to provide up to 10 mJ of energy to the desired target, but could only irradiates a section of the sample without rotation (Fig. 1.e). We have also done preliminary work with a commercially available, conical-tip fiber that allows for full 360° irradiation (Fig. 1.f). This fiber tip
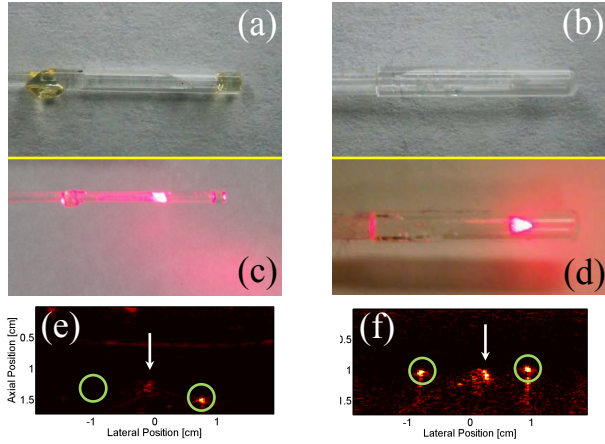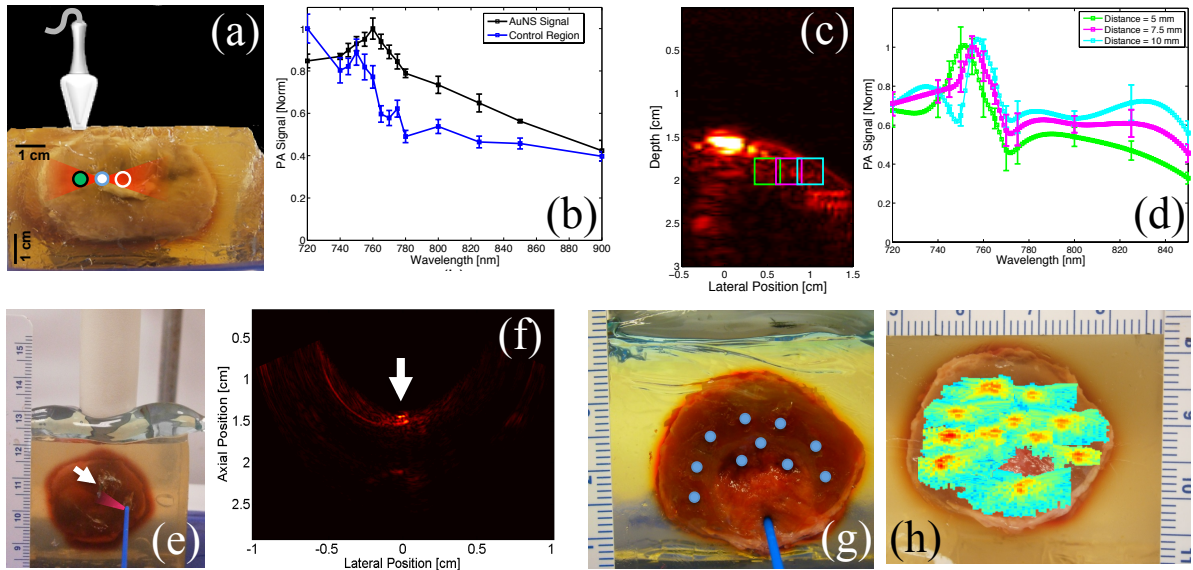
Fig. 1: (a) Photo of capped side-fire fiber tip. (b) Photo of conical-tip fiber. (c) Irradiation pattern from side-fire tip. (d) Irradiation pattern from conical tip. (e) PA image of one wire (green circles) using side-fire fiber (white arrow). (f) PA image of two wires using conical-tip fiber.
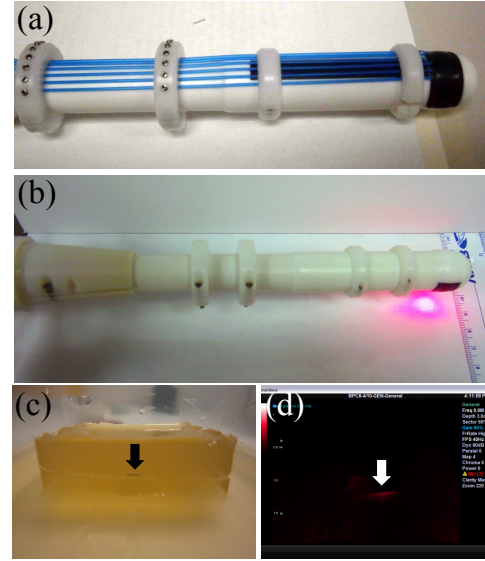
allows for imaging within the full plane, rather than the quadrants provided from side-fire imaging. In a preliminary study with two embedded wire targets (denoted with green circles in Fig. 1.e,f), the conical-tip fiber produced a consistent signal in both targets regardless of the rotation of the fiber, while the side-fire fiber exhibited a strong directional dependence when imaging.

To demonstrate *ex vivo* application of PA imaging driven with interstitial irradiation, excised bovine prostate tissue was encased in gelatin, and then injected with gold nanospheres (AuNS's) to provide an imaging target (Fig. 2.a). After injection, a side-fire irradiation fiber was inserted into the phantom and used to generate PA images of the prostate in both AuNS-containing regions (black/green oval) and non-injected control regions (white oval). sPA imaging was then performed at wavelengths between 720 and 900 nm and analyzed to determine the PA spectra (which is related to the optical absorption spectrum) of the imaging targets (Fig. 2.b). The PA spectrum in the region injected with AuNS's (black trace in Fig. 2.b) peaked at 760 nm, which is consistent with their optical absorption spectrum (Fig. 2.d). However, in the non-injected control region, the PA signal spectrum (blue trace in Fig. 2.b) was consistent with the optical absorption spectrum of deoxyhemoglobin (HHb). The rest of Fig. 2 shows an image (2.c) and PA spectral data (2.d) from an imaging


Fig. 2: (a,e,g) Imaging setups. (b) AuNS (black) and HHb (blue) PA spectra from (a). (f) PA image of wire target (arrow) from (e). (d) Spectra acquired from ROIs in (c). (h) PA imaging data – thresholded for noise – acquired from (g) and overlaid a photo.

5

experiment with interstitial irradiation in excised bovine liver tissue. In the PA image (2.c), three analysis kernels (at distances 5 [lime trace], 7.5 [magenta trace], & 10 [cyan trace] mm away from the source) are denoted in which the average PA signal was calculated for each wavelength acquired (ranging from 720-850 nm). The spectra are generally consistent with the absorption spectrum of HHb; however, there is a slight redshift of approximately 3 nm per 2.5 mm increase in distance from the irradiation source due to wavelength-dependent scattering. This experiment highlights the necessity for more proximal irradiation if photoabsorbers are to be accurately characterized based on their PA spectra. Fig. 2.e offers a photograph of the TRUS transducer imaging excised bovine prostate with an imbedded wire target (white arrow) and driven with interstitial irradiation (blue line); the accompanying PA image (2.f)

Figure 3 – (a) PA-TRUS side-fire probe. (b) Optical irradiation volume from probe fibers. (c) Phantom containing prostate brachytherapy seed. (d) PA image of brachytherapy seed.

clearly shows the wire target. Lastly, Fig. 2.g shows a mock biopsy with 11 irradiation sites (blue) in bovine prostate and the resulting PA signal (Fig. 2.h) obtained at 760 nm. Note that 11 interrogations is able to sample the majority of the gland's cross-section.
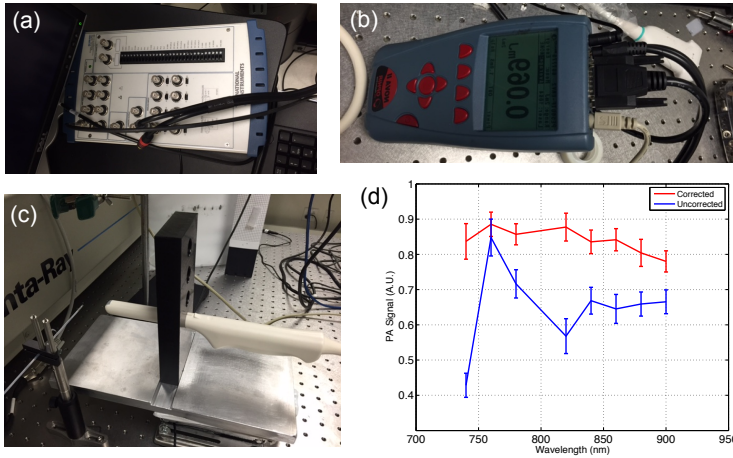
Fig. 4: (a) LabVIEW acquisition unit with analog inputs, (b) energy meter, and (c) tranarectal probe with holder and fiber mount. (d) Wire energy correction validation.

Additionally, we integrated seven side-fire fibers onto the shaft of a BPL9-5/55 TRUS probe (Fig. 3.a,b) that was connected to a Sonix RP ultrasound system (Ultrasonix, Burnaby, BC, Canada). These optical fibers were then coupled into a pulsed Pro-270-10 Nd:YAG laser (Spectra-Physics, Santa Clara, CA), then used to deliver light coincident to the US imaging plane (Fig. 3.b) to generate PA images of brachytherapy seeds within gelatin (Fig. 3.c) and tissue-mimicking phantoms; a preliminary PA image (Fig. 3.d) generated by the custom PA-TRUS probe shows a brachytherapy seed imaged at approximately 1.2 cm depth. Although interstitial irradiation should provide sufficient SNR, external irradiation could be used as a supplement to increase overall fluence.

In an effort to provide pulse-to-pulse energy correction, a beam splitter was placed before the fiber input and directed toward an energy meter (4.b). The analog output from
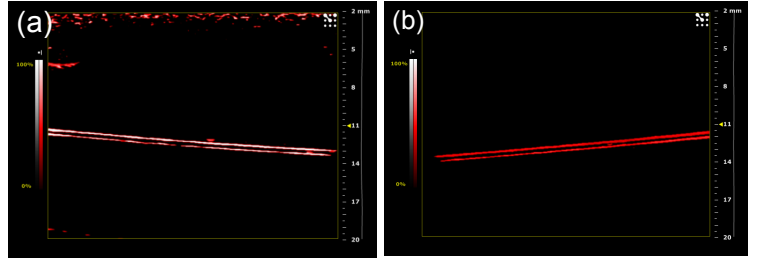
this meter was then input into a LabVIEW data acquisition (4.a) module to allow for pulse-to-pulse correction of energy with an imaging frame. Using this energy correction, we were able to achieve a flat response for a metal wire (4.d) with reduced signal variation at each wavelength tested. Finally, a Delrin transducer holder with multiple translation/rotation ports was mounted on a stainless steel baser (4.c) to allow precision adjustment of the transrectal probe relative to the fiber source. The mount allows for controlled rotation and translation of the probe.

The presence of the HHb PA signal provides a biomarker for locating aggressive prostate cancer. Spectral unmixing to differentiate HHb and oxyhemoglobin (HbO_2) PA signal is achieved using inverse analysis applied to physics-based models of the reconstruction. Modeling the reconstruction involves: estimating the initial pressure distribution from the absorbed light source and propagating the acoustic wave from the initial pressure distribution to the ultrasound receiver hardware. An information theoretic mathematical framework for adaptive sampling and identifying wavelength and SNR acquisition parameters that provide the most information content with respect to the physics model based data collection was utilized. The interface, which is driven my MATLAB, allows the operator to denote needle insertion points within the global DICOM frame. GPU kernels are provided to compute intensive elements of the pipeline to enable high throughput processing.

In an effort to assess oxygen saturation techniques, PA imaging was also conducted on heparinized ex-vivo bovine blood at differing sO_2 levels, as confirmed by an independent blood gas analyzer. To achieve desired sO_2 levels, the bovine blood was subjected to an environment of pure oxygen or pure nitrogen to ensure all

Fig. 5: (a) PA image of sample tube filled with blood. Blood gas analysis places SO_2 at 100% in this image, PA-based methods estimate an sO_2 of 95%. (b) PA image of sample tube filled with partially HHb blood. SO_2 is estimated at 60% in this image.

available hemoglobin was in the desired oxygenation state (i.e., fully oxygenated or HHb, respectively). This blood was then drawn and mixed with blood from the other oxygenation state in appropriate proportions to create differing oxygenation levels. This blood was then injected into a phantom consisting of an acrylic shell with holes milled at equal depths holding 1 mm outer diameter polyethylene tubing. The void within the phantom surrounding the tubes was filled with water; however this space can also be filled with tissue-mimicking phantom material to translate the values to future in vivo models. Using the Vevo 2100 LAZR system (Verasonics Inc., Toronto, Canada), the ratio of PA signal at 850 vs 750 nm was calculated for each oxygenation concentration (Fig. 5) to achieve ratiometric sO_2 estimation. These values were then matched to independent sO_2 measurements from the blood gas analysis to allow the ratiometric value obtained from imaging to be mapped to a known sO_2 level. In initial studies, the ratiometric method has presented an ~5% bias in underestimating the oxygen saturation.

To establish a more quantitative method to assess sO_2 in the future, tradeoffs between accuracy in the physics based predictions and numerical efficiency are considered within

the context of the model-based reconstruction (Fig. 6). A key idea of our approach is that clinically significant spatial variations of sO₂ may be detected using the appropriate numerical approximations, i.e., full numerical solution to the coupled partial differential equations that govern the inherent fluence and pressure for photoacoustic detection are not needed. A more thorough detailing of this work and the underlying mathematical framework is included in the appendix.
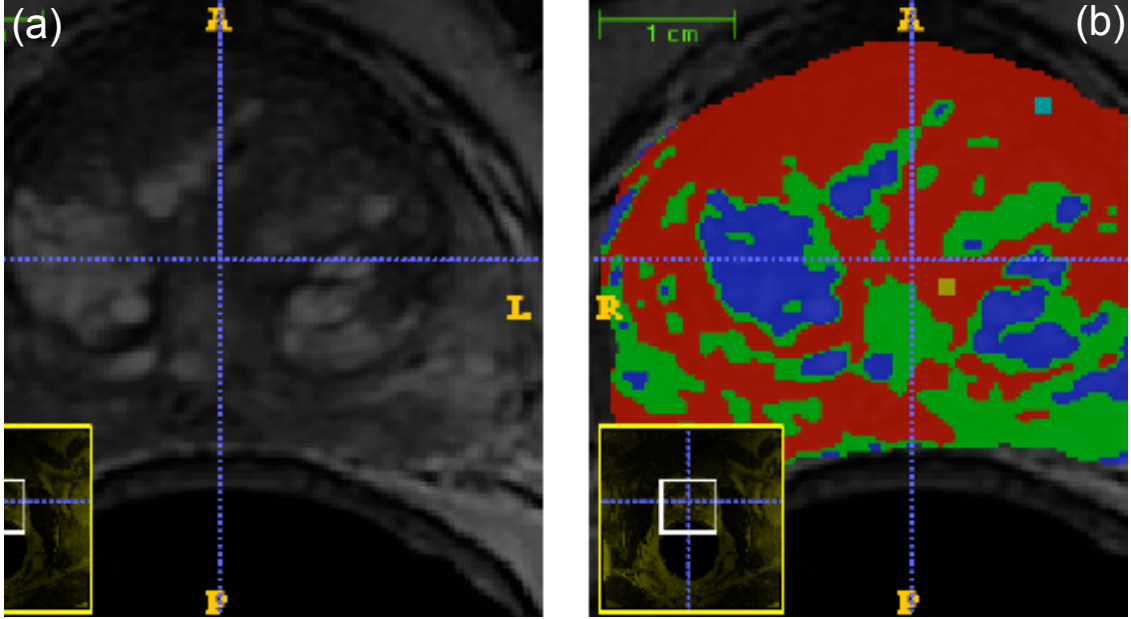
Fig. 6: The spatial decomposition is given by a three-constituent Gaussian mixture model (b) applied to pre-procedural imaging (a). The label map also encodes the laser applicator location.

3) Other Achievements
In addition to prostate imaging, we have also successfully imaged in excised liver, characterizing the PA-based spectrum of HHb to a depth of beyond 7 cm from the US transducer face. We have also characterized the red-shift that results from wavelength-dependent attenuation in the prostate; this shift can confound PA-based oxygen saturation estimation. We have also investigated the bias associated with conventional SO₂ estimation methods.

4) Stated Goals Not Met
All stated goals have generally been met. Ultimately, we chose to implement a probe positioning option that incorporated known fiber positions into the spatial localization system instead of relying on encoder information. It was brought to our attention by our clinical collaborator that a commercial-grade spatial location system will be required for future clinical trials. Thus, we feel that our precision-milled Delrin holder will allow us to continue preclinical development and optimization until it is possible to partner with a commercial entity that can provide the precision required for clinical translation. Recently, we have secured a letter of support from a commercial partner for such collaboration.

Training:
Trevor Mitcham, BS, the original research assistant (RA) assigned to the project received one-on-one mentorship from Richard Bouchard, PhD, on photoacoustic imaging development and optimization. Mr. Mitcham was then inspired – due in part to his interest in the project – to enroll in the University of Texas Graduate School of Biomedical Sciences program in Medical Physics. Houra Taghavi, MS, then took over Mr. Mitcham's (RA) duties on the project; she also received one-on-one mentorship from Dr. Bouchard on photoacoustic imaging development and optimization.

How Results Were Disseminated:
Results from this research have been disseminated via a peer-reviewed publication and four conference presentations.

Peer-reviewed Publication:
1. Mitcham T, Dextraze K, Taghavi, H, Melancon M, Bouchard R. "Photoacoustic imaging driven by an interstitial irradiation source," *Photoacoustics*, 2015. (included in appendix)

Conference Presentations:
1. Bouchard RR. "Advances in Ultrasound-Mediated Imaging," *American Association of Physicists in Medicine Southwest Chapter Spring Meeting*, 2014.
2. Mitcham T, Dextraze K, Karipouk A, Singhana B, Melancon M, Bouchard R. "Increasing the penetration depth of clinical photoacostic imaging with interstitial irradiation," *39th International Symposium on Ultrasonic Imaging and Tissue Characterization*, 2014.
3. Bouchard R, Thornton M, Dextraze K, Morgan T, Grant J, Krishnan S. "Coregistered photoacoustic perfusion assessment and targeted nanoparticle tracking in a prostate cancer model," *39th International Symposium on Ultrasonic Imaging and Tissue Characterization*, 2014.
4. Mitcham T, Lynch J, Cook J, Emelianov S, **Bouchard R**. "Development and Characterization of a Temporally Stable Tissue-Mimicking Photoacoustic-Ultrasonic Phantom," *American Association of Physicists in Medicine 56th Annual Meeting and Exhibition*, 2014.
5. Bouchard RR. "Clinical Opportunities for Photoacoustic-Ultrasonic Imaging," *Medical Physics Lecture Series at the German Cancer Research Center, Heidelberg, Germany*, 2015.
6. Mitcham T, Guha S, Dextraze K, Lee A, Sokolov K, Smith B, **Bouchard R**. "Environmentally-sensitive contrast agents for photoacoustic imaging of cancer cells," *40th International Symposium on Ultrasonic Imaging and Tissue Characterization*, 2015

Plans for Next Reporting Period:
N/A

4. Impact

<u>Impact on the development of the principal discipline(s) of the project:</u> This research demonstrates that interstitial irradiation with an external ultrasound imaging source permits deep interrogation in soft tissue, with PA images made in liver at depths in excess of 7 cm. This increased interrogation depth from an interstitial source makes additional clinical, interventional radiology applications feasible targets for future translation of PA imaging. This work also demonstrates the bias and confounding effects of SO_2 measurements.

<u>Impact on other disciplines:</u> Nothing to report.

<u>Impact on technology transfer:</u> Nothing to report.

<u>Impact on society beyond science and technology:</u> Nothing to report.

5. Changes/Problems

Actual or anticipated problems or delays and actions or plans to resolve them: Initially, there were issues with the previous imaging system (i.e., not truly real-time) and the quality of the interstitial fibers produced in-house. To remedy the first issue, we switched to an entirely new imaging platform – the Verasonics ultrasound imaging system – which allows us to provide real-time, interstitially driven PA imaging. To remedy the second issue, we collaborated with Pioneer Optics to repurpose photodynamic therapy fibers for our application. Not only has this improved production quality, but it has also allowed for a greater irradiation volume over side-fire fibers. The final issue, as has been previously described, involved the use of encoders to determine position. Instead, we chose to provide this information with the known position of the fibers themselves (i.e., through coordinates from an implantation grid) and are pursuing a more robust commercial option for future preclinical trials.

6. Products: Nothing to report**.**

7. Participants & Other Collaborating Organizations

Name:	Richard Bouchard, PhD
Project Role:	Principal Investigator
Nearest Person Month Worked:	3.0
Contribution to Project:	Lead the fabrication/integration of all system components. Generally, responsible for the overall direction and conduct of the proposed program, overseeing all day-to-day activities.

Name:	David Fuentes, PhD
Project Role:	Co-Investigator
Nearest Person Month Worked:	0.6
Contribution to Project:	Developed model-based rendering tools to allow for precise PA-based oxygen saturation maps.

Name:	John Ward, MD
Project Role:	Co-Investigator
Nearest Person Month Worked:	0.12
Contribution to Project:	Provided clinical perspective to ensure prototype and transrectal imaging system were clinically translatable.

Name:	Trevor Mitcham, BS
Project Role:	Research Assistant
Nearest Person Month Worked:	2.5
Contribution to Project:	Assisted in data processing and adaptive needle/system optimization (during prototype development). Fabricated side-fire fibers and integrated with PA imaging system. Developed and imaged gelatin and tissue phantoms.

Name:	Houra Taghavi, BS
Project Role:	Research Assistant
Nearest Person Month Worked:	4.5
Contribution to Project:	Assisted in data processing and adaptive needle/system optimization (during prototype development). Fabricated side-fire fibers and integrated with PA imaging system. Developed and imaged gelatin and tissue phantoms. Integrated LabVIEW and MATLAB features with imaging hardware. Developed probe holder.

8. Special Reporting Requirements: Nothing to report**.**

9. Appendices (see attachments)

PA Recon

David Fuentes

April 12, 2015

The presence of deoxyhemoglobin PA signal provides a biomarker for locating aggressive prostate cancer. Spectral unmixing to differentiate deoxy- (HHb) and oxyhemoglobin (HbO2) PA signal is achieved using inverse analysis applied to physics based models of the reconstruction. Modeling the reconstruction involves: (Section 2) estimating the initial pressure distribution from the absorbed light source and (Section 3) propagating the acoustic wave from the initial pressure distribution to the ultrasound receiver hardware. An information theoretic mathematical framework for adaptive sampling and identifying wavelength and SNR acquistion parameters that provide the most information content with respect to the physics model based data collection is presented in Section 1. The MATLAB script `exampleRecon.m` documents the user interface developed, Section 4. The interface allows the operator to denote needle insertion points within the global DICOM frame. GPU kernels are provided for compute intensive elements of the pipeline to enable high throughput processing.

Tradeoffs between accuracy in the physics based predictions and numerical efficiency are considered within the context of the model-based reconstruction. A key idea of our approach is that clinically significant spatial variations of sO2 may be detected using the appropriate numerical approximations. Ie, full numerical solution to the coupled partial differential equations that govern the inherent fluence and pressure for photoacoustic detection are not needed.

1 Mathematical Framework

The underlying philosophy and assumptions within our approach is that the physics models are 1st order accurate or within 70-80% of the needed accuracy and the error is adequate within the assumed Gaussian noise. Gaussian distributions provide analytical representations of the random variables of interest (ie volume fraction of HHb, ϕ) within the Bayesian setting and provide a crux for understanding. In particular, we say that a random variable η belongs to a multi-variate normal distribution of mean $\mu \in \mathbb{R}^n$ and covariance $\Sigma \in \mathbb{R}^{n \times n}$

$$\eta \sim \mathcal{N}(\mu, \Sigma) \Rightarrow p(\eta) = \frac{1}{2\,\pi\,\det\Sigma} \exp\left(-\frac{1}{2}\|\mu - \eta\|_\Sigma^2\right)$$

1. Our data acquistion model, $\mathcal{G}(\vec{k}, \theta) : \mathbb{R}^a \times \mathbb{R}^m \to \mathbb{R}^n$, maps deterministic acquisition parameters, $\vec{k} \in \mathbb{R}^a$, and uncertain parameters, $\theta \in \mathbb{R}^m$ to observables, $\vec{z} \in \mathbb{R}^n$ (or $\vec{z} \in \mathbb{C}^n$). Explicitly, we will assume that the measurement models are corrupted by zero mean white noise noise of a **known** covariance matrix, $\Sigma_z \in \mathbb{R}^{n \times n}$

$$
\begin{aligned}
\vec{z} &= \mathcal{G}(\vec{k}; \theta) + \eta \qquad \eta \sim \mathcal{N}(0, \Sigma_z) \\
\vec{k} &= \text{(frequency, laser position, etc)} \\
\theta &= \text{(volume fraction, absorption, etc)}
\end{aligned}
\tag{1}
$$

η may be interpreted as the measurement noise or the acquisition noise in the sensor model. For a deterministic measurement model $\mathcal{G}$, the conditional probablity distribution has an explicit analytical form and may be written as a **known** Gaussian distribution.

$$p(\vec{z}|\theta) = \mathcal{N}(\mathcal{G}(\vec{k}; \theta), \Sigma_z)$$

2. Additional **known** information is the prior probability distributions for the model parameters, $p(\theta)$. For simplicity, assume that Prior parameters are Gaussian distributed of **known** mean, $\hat{\theta}$ and covariance, Σ_θ

$$\theta \sim \mathcal{N}(\hat{\theta}, \Sigma_\theta)$$

3. Bayes theorem is fundamental to the approach. The probability of the measurements $p(z)$ must be interpreted in terms of the known information. The probability of the measurements may be derived from the marginalization of the joint probability and has the interpretation as the projection of the joint probability onto the measurement axis.

$$p(z) = \int_\theta p(\theta, z)\, d\theta = \int_\theta p(z|\theta)\, p(\theta)\, d\theta$$

4. The concept of informational entropy [Madankan et al., 2015], $H(Z)$, provides a mathematically rigorous framework to look for measurement acquisition parameters, $\vec{k}$, with the high information content of the reconstruction. Given a probability space $(\Omega, \mathcal{F}, p)$ (probability maps from the sigma-algebra of possible events $p : \mathcal{F} \to [0, 1]$ sigma-algebra, $\mathcal{F}$, defined on set of 'outcomes' Ω [Durrett, 2010]), we will define information of an event as proportional to the inverse probability.

$$\text{information} \equiv \frac{1}{p(z)}$$

Intuitively, when a low probability event occurs this provides high information. The informational entropy is an *average* of the information content for a sigma algebra of events $\mathcal{F}$

$$H(Z) = \int_Z p(z) \ln \frac{1}{p(z)}\, dz \qquad p(z) = \int_\theta p(z|\theta)\, p(\theta)\, d\theta$$

Hence this entropy measure is an average of the information content for a given set of events, $\mathcal{F}$, and is proportional to the variance or uncertainty in which the set of events occur. This agrees with thermodynamic entropy; if the information containing events are completely spread out such as in a uniform distribution, the entropy is maxmized. The entropy is zero for a probability distribution in which only one event occurs. Zero information is gained when the same event always occurs ($0 \ln \frac{1}{0} = 0$). Intuitively, we want to find acquisition parameters, $\vec{k}$, for which the measurements are most uncertain

$$\max_k H(Z) \quad \Leftrightarrow \quad \min_k \int_Z dz \underbrace{\int_\theta d\theta\, p(z|\theta)\, p(\theta)}_{p(z)}\, ln \underbrace{\left(\int_\theta d\theta\, p(z|\theta)\, p(\theta) \right)}_{ln\, p(z)}$$

Alternatively we may consider this entropy maximization problem as a sensitivity analysis for the variance of the measurement Z, ie . $\max_k H(Z) \approx \max_k \text{Var}(Z)$

$$\bar{Z} = \mathbb{E}[Z] = \int_Z dz\, z \underbrace{\int_\theta d\theta\, p(z|\theta)\, p(\theta)}_{p(z)}$$

$$\mathbb{E}[(Z - \bar{Z})^2] = \int_Z dz\, (z - \bar{Z})^2 \underbrace{\int_\theta d\theta\, p(z|\theta)\, p(\theta)}_{p(z)}$$

$$\propto \int_Z dz\, (z - \bar{z})^2 \int_\theta d\theta \exp\left(-\frac{1}{2}\|z - \mathcal{G}(\vec{k}, \theta)\|^2_{\Sigma_z} \right) \exp\left(-\frac{1}{2}\|\theta - \hat{\theta}\|^2_{\Sigma_\theta} \right)$$

Probilistic integrals may be computed from uncertainty quantification techniques [Fahrenholtz et al., 2013].

2 Fluence Source

Reconstruction methods incorporate the spatial distribution of the absorption and scattering into the expected time dependent photo-acoustic signal of a single wavelength excitation. Diffusion-based light transport models in turbid media as well as directional models of light propagation using considerations of the delta-Eddington phase function are available [MacLellan et al., 2013, Fuentes et al., 2013, Fuentes et al., 2010, Fuentes et al., 2009]. A key idea of the inverse analysis is that the optical absorption provides the image contrast within the spectral unmixing. Within our application, the optical absorption, μ_a, is considered a linear combination of the volume fractions, ϕ, of deoxy- (HHb) and oxyhemoglobin (HbO2) constituents.

$$\mu_a(\lambda, x) = \phi(x)\mu_a^{\text{HHb}}(\lambda) + (1 - \phi(x))\mu_a^{\text{HbO2}}(\lambda)$$

Spatial variations in the optical absorption are directly related to hypoxic regions and will be detected by exploiting the frequency dependence of the optical properties. Spatial variations in optical parameters are considered as the spatial decomposition of the prostate domain, Ω

$$\Omega = \cup_j \Omega_j \qquad \Omega_i \cap \Omega_j = \emptyset \quad i \neq j \qquad \psi_j(x) = \begin{cases} 1 & x \in \Omega_j \\ 0 & x \notin \Omega_j \end{cases} \qquad \phi(x) = \sum_{j=1}^{N_\phi} \phi_j \psi_j(x)$$

Within the context of our mathematical framework, Section 1, the volume fraction mixing parameter and the optical parameters are uncertain model variables, θ. The wavelength is the deterministic acquisition parameters, $\vec{k}$. we have little information about the mixing parameter ϕ and will consider this to be uniformly distributed. Optical absorption is both species and wavelength dependent. We assume that the optical parameters is Gaussian distributed about the mean of the tabulated spectrum.

$$\phi_j \sim \mathcal{U}(0,1) \qquad \mu_a^{\text{HHb}}(\lambda) \sim \mathcal{N}\left(\bar{\mu}_a^{\text{HHb}}(\lambda), \Sigma_{\mu_a}\right) \qquad \mu_a^{\text{HbO2}}(\lambda) \sim \mathcal{N}\left(\bar{\mu}_a^{\text{HbO2}}(\lambda), \Sigma_{\mu_a}\right)$$

$$\theta = \left(\phi_1, ..., \phi_{N_\phi}, \mu_a^{\text{HHb}}(\lambda), \mu_a^{\text{HbO2}}(\lambda)\right) \qquad \vec{k} = \lambda$$

2.1 Standard Diffusion Approximation

The starting point for modeling light transport in tissue is the Boltzman equation for the radiance, $L(\mathbf{r}, \hat{s})$.

$$\hat{s} \cdot \nabla L(\mathbf{r}, \hat{s}) + \mu_t(\mathbf{r}) L(\mathbf{r}, \hat{s}) = \mu_s \int_{4\pi} p(\hat{s}, \hat{s}') L(\mathbf{r}, \hat{s}) \, d\omega \qquad \mu_t = \mu_a + \mu_s \tag{2}$$

Here the radiance, $L(\mathbf{r}, \hat{s})$, represents the radiant power per unit of solid angle about unit vector $\hat{s}$ and per unit area perpendicular $\hat{s}$. The Boltzman equation represents a conservation of energy applied to light energy transport in tissue at point r. The phase function, $p(\hat{s}, \hat{s}')$, provides a measure of the probability of a scattering photons traveling in direction $\hat{s}'$ into the direction $\hat{s}$. The mean cosine of the scattering angle is known as the anisotropy factor, g

$$\int_{4\pi} p(\hat{s} \cdot \hat{s}')(\hat{s} \cdot \hat{s}') d\omega' \equiv g$$

By convention, the radiance is considered as the summation of a *known* primary light source with irradiance, $E(\mathbf{r})$, traveling in direction s_0 and scattered light source.

$$L(\mathbf{r}, \hat{s}) = L_p(\mathbf{r}, \hat{s}) + L_s(\mathbf{r}, \hat{s}) = \frac{E(\mathbf{r})\delta(1 - \hat{s} \cdot \hat{s}_0)}{2\pi} + L_s(\mathbf{r}, \hat{s})$$

The scattered radiance may be represented as sum of spherical harmonics, this is known as the P-n approximation[Welch and Van G Modest, 2013].

$$L_s(\mathbf{r}, \hat{s}) = \sum_i^\infty L_i(\mathbf{r}) P_i(\hat{s})$$

When only the first two terms are used, this is known as the P-1[Modest, 2013] or diffusion approximation[Modest, 2013].

$$L_s(\mathbf{r}, \hat{s}) \approx \frac{1}{4\pi} \varphi_d(\mathbf{r}) + \frac{3}{4} \mathbf{j}(\mathbf{r}) \cdot \hat{s} \tag{3}$$

When i=0,1,2,3 terms are kept, this is known as the P-3 approximation. The P-2 approximation is generally less accurate and not used[Modest, 2013].

The diffusion model for light transport is valid under the assumption that light is scattered more than absorbed.

$$\mu_a << \mu_s(1 - g) \Rightarrow \mu_{eff} << \mu_t$$

The PDE for the SDA is obtained in two steps by (i) substituting (3) into (2) and integrating over all solid angles and (ii) multipling (2) by $\hat{s}$ and integrating over all solid angles. Combining the result yeilds

$$\nabla \cdot \left(\frac{1}{3\mu_{tr}} \nabla \varphi_d(\mathbf{r})\right) - \mu_a \varphi_d(\mathbf{r}) = -\mu_s E(\mathbf{r}) + \nabla \cdot \left(\frac{g\mu_s}{\mu_{tr}} E(\mathbf{r})\hat{s}_0\right) \qquad \mu_s' = \mu_s(1 - g) \quad \mu_{tr} = \mu_a + \mu_s'$$

$$\mathbf{j}(\mathbf{r}) = \frac{-1}{3\mu_{tr}} \left[\nabla \varphi_d(\mathbf{r}) - 3g\mu_s E(\mathbf{r})\hat{s}_0\right] \qquad \mu_{eff} = \sqrt{3\mu_a \mu_{tr}}$$

$\mathbf{j}$ is the radiant flux, $\hat{z}$ is the direction of the collimated light, etc...

3

2.2 Homogenious Coefficients

Through the diffusion model, the scattered fluence z is obtained from the known irradiance $E(x,t)$ (primary source of photons) and its flux $\mathbf{F}(x,t)$ [Fuentes et al., 2011]. The total fluence at a point is given by the sum of the scattered and primary light $\varphi_t(x,t) = z(x,t) + E(x,t)$. The irradiance is provided by a photon flux emitted throughout the domain of an interstitial laser fiber Ω_{tip}. The photons are emittied by an applied power density, $P^* \left[\frac{W}{m^3} \right]$. Each position in the domain $\hat{x} \in \Omega_{tip}$ is treated as a point source of irradiance

$$dE(x, \hat{x}) = \frac{P^*(t)d\hat{x}}{4\pi \|\mathbf{x} - \hat{\mathbf{x}}\|^2}$$

The total irradiance and flux is the integral of each attenuated point source.

$$E(x,t) = \int_{\Omega_{tip}} \frac{P^*(t)}{4\pi \|\mathbf{x} - \hat{\mathbf{x}}\|^2} \exp\left(\mu_t^*(\mathbf{x}, m) \|\mathbf{x} - \hat{\mathbf{x}}\| \right) d\hat{x}$$

$$\mathbf{F}(x,t) = \int_{\Omega_{tip}} \frac{P^*(t)}{4\pi \|\mathbf{x} - \hat{\mathbf{x}}\|^2} \exp\left(\mu_t^*(\mathbf{x}, m) \|\mathbf{x} - \hat{\mathbf{x}}\| \right) \frac{\mathbf{x} - \hat{\mathbf{x}}}{\|\mathbf{x} - \hat{\mathbf{x}}\|} d\hat{x}$$

$$\mu_t^*(\mathbf{x}, m) = \mu_a(\mathbf{x}, m) + \mu_s(\mathbf{x}, m)$$

An analytic solution may be obtained by approximating the integral for the irradiance and flux as

$$E(x,t) \approx \sum_{e \in \Omega_{tip}} E_e(x,t) = \sum_{e \in \Omega_{tip}} \frac{\Delta V_e P^*(t)}{4\pi \|\mathbf{x} - \hat{\mathbf{x}}_e\|^2} \exp\left(\mu_t^*(\mathbf{x}, m) \|\mathbf{x} - \hat{\mathbf{x}}_e\| \right)$$

$$\mathbf{F}(x,t) \approx \sum_{e \in \Omega_{tip}} \mathbf{F}_e(x,t) = \sum_{e \in \Omega_{tip}} \frac{\Delta V_e P^*(t)}{4\pi \|\mathbf{x} - \hat{\mathbf{x}}\|^2} \exp\left(\mu_t^*(\mathbf{x}, m) \|\mathbf{x} - \hat{\mathbf{x}}\| \right) \frac{\mathbf{x} - \hat{\mathbf{x}}}{\|\mathbf{x} - \hat{\mathbf{x}}\|}$$

where ΔV_e is the volume and $\hat{\mathbf{x}}_e$ is the centroid. By linearity, each element in the discretization may be treated as an uncoupled and independent source in the light diffusion equation.

$$-\mu_a(\mathbf{x})z_e + \mu_s^*(\mathbf{x}, m)E_e = \nabla \cdot \left(-\frac{\nabla z_e}{3\mu_{tr}(\mathbf{x}, m)} + \frac{\mu_s^*(\mathbf{x}, m)g^*}{3\mu_{tr}(\mathbf{x}, m)} (\mathbf{F})_e \right) \qquad \forall e \in \Omega_{tip}$$

The fluence resulting from each element source $(\varphi_t)_e$ may be obtained from the classical isotropic point source solution [Welch and Van Gemert, 1995]. The total emanating fluence is the superposition of the element wise solutions and reduces to a volume weighted sum over the elements.

$$\varphi_t = \sum_{e \in \Omega_{tip}} P^*(t)V_e \left(\frac{3\mu_{tr} \exp(-\mu_{eff}\|\mathbf{x} - \mathbf{x}_e\|)}{4\pi \|\mathbf{x} - \mathbf{x}_e\|} - \frac{\exp(-\mu_t^*\|\mathbf{x} - \mathbf{x}_e\|)}{2\pi \|\mathbf{x} - \mathbf{x}_e\|^2} \right) \approx \sum_{e \in \Omega_{tip}} P^*(t)V_e \frac{3\mu_{tr} \exp(-\mu_{eff}\|\mathbf{x} - \mathbf{x}_e\|)}{4\pi \|\mathbf{x} - \mathbf{x}_e\|}$$

$$\mu_{eff}(\mathbf{x}, m) = \sqrt{3\mu_a(\mathbf{x}, m)\mu_{tr}(\mathbf{x}, m)}$$

3 Wave Propagation

Computer models of the partial differential equation governing the propagation of the acoustic wave are expensive. Approximations using k-space methods and greens function techniques for back projection will be utilized....

4 User Interface

Example code and user interface is provided from the project site, `https://github.com/ImageGuidedTherapyLab/PALikelihoodMap`. GPU kernels use a grid stride loop design pattern for compute intensive physics model calculations. The MATLAB script `exampleRecon.m` computes the wavelength sensitivity in two steps.

1. Uncertainty quantification techniques are applied to compute the variance of the photoacoustic source, Section 1 and Section 2.

2. Sensitivity statistics are propagated through our photo acoustic model for the wave propagation, Section 3.

The SDA fluence model is proportional to photoacoustic source, $S(r) \left[\frac{W}{m^3}\right]$, with a proportionality constant given by the *dimension-less* Gruneisen parameter, $\Gamma = \frac{v_s^2 \beta}{c_p}$

$$\text{PA source} = S(r) = \Gamma \mu_a \varphi_t \propto \sum_e P^*(t) V_e \frac{\mu_{eff}^2 \exp(-\mu_{eff}(\mathbf{x})\|\mathbf{x}-\mathbf{x}_e\|)}{4\pi \|\mathbf{x}-\mathbf{x}_e\|}$$

$$\mu_{eff} = \sqrt{3\mu_a \mu_{tr}} \quad \mu_{tr} = \mu_a + \mu_s(1-g)$$

$$\mu_a(\lambda, x) = \phi(x)\mu_a^{\text{HHb}}(\lambda) + (1-\phi(x))\mu_a^{\text{HbO2}}(\lambda)$$
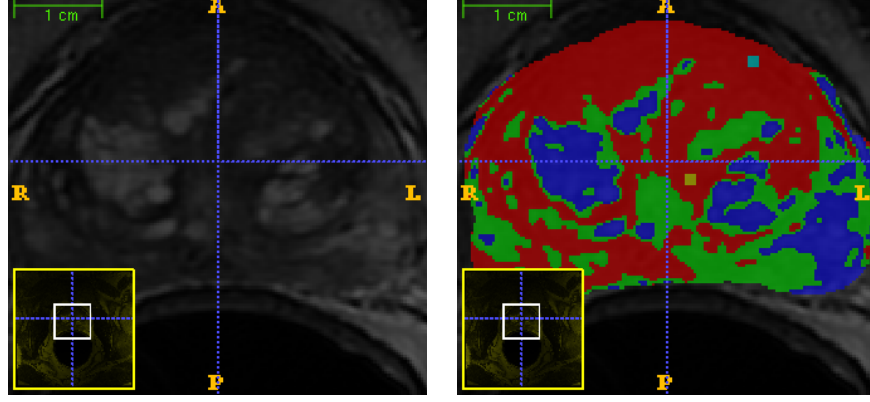
$$\Omega = \cup_j \Omega_j \qquad \Omega_i \cap \Omega_j = \emptyset \quad i \neq j \qquad \psi_j(x) = \begin{cases} 1 & x \in \Omega_j \\ 0 & x \notin \Omega_j \end{cases} \qquad \phi(x) = \sum_{j=1}^{N_\phi = 3} \phi_j \psi_j(x)$$

Figure 1: The spatial decomposition is given by a three constituent Gaussian mixture model applied to pre-procedural imaging. The label map also encodes the laser applicator location (Label = 4 = applicator centroid, Label = 5 = entry point).

Assuming each parameter is independent, the parameter space probability function is the tensor product of the individual distributions.

$$\theta = \left(\phi_1, ..., \phi_3, \mu_a^{\text{HHb}}(\lambda), \mu_a^{\text{HbO2}}(\lambda)\right)$$

$$\mu_a = \left(\theta_1 \psi_1(x) + \theta_2 \psi_2(x) + \theta_3 \psi_3(x)\right)\theta_4 \qquad p(s|\theta) = \frac{1}{\sqrt{2\pi \Sigma_s}} \exp^{-\frac{(s - \Gamma \mu_a \varphi_t)^2}{2 \Sigma_s}}$$
$$+ \left(1 - \theta_1 \psi_1(x) + \theta_2 \psi_2(x) + \theta_3 \psi_3(x)\right)\theta_5$$

$$p(\theta) = \underbrace{\frac{1}{}}_{\mathcal{U}(0,1)} \cdot \underbrace{\frac{1}{}}_{\mathcal{U}(0,1)} \cdot \underbrace{\frac{1}{}}_{\mathcal{U}(0,1)} \cdot \underbrace{\frac{1}{\sqrt{2\pi \Sigma_{\mu_a}}} \exp^{-\frac{(\theta_4 - \bar{\mu_a}^{\text{HHb}}(\lambda))^2}{2\Sigma_{\mu_a}}}}_{\mathcal{N}(\bar{\mu_a}^{\text{HHb}}(\lambda), \Sigma_{\mu_a})} \cdot \underbrace{\frac{1}{\sqrt{2\pi \Sigma_{\mu_a}}} \exp^{-\frac{(\theta_5 - \bar{\mu_a}^{\text{HbO2}}(\lambda))^2}{2\Sigma_{\mu_a}}}}_{\mathcal{N}(\bar{\mu_a}^{\text{HbO2}}(\lambda), \Sigma_{\mu_a})}$$

Table 1: Constitutive Data used in numerical simulations [Welch, 1984, Duck, 1990]

$\bar{\mu_a}^{\text{HHb}}(750nm) \frac{1}{m}$	$\bar{\mu_a}^{\text{HHb}}(850nm) \frac{1}{m}$	$\bar{\mu_a}^{\text{HbO2}}(750nm) \frac{1}{m}$	$\bar{\mu_a}^{\text{HbO2}}(850nm) \frac{1}{m}$	g	$\mu_s \frac{1}{cm}$	$\sqrt{\Sigma_{\mu_a}} \frac{1}{m}$	Γ
7.e2	4.e2	5.e2	6.e2	0.9	140.e2	1.e1	.45

Uncertainty quantification techniques [Fahrenholtz et al., 2013] are used to evaluate sensor model statistics.

$$\bar{S}(\lambda) = \mathbb{E}[S] = \int_S ds \, s \underbrace{\int_\theta d\theta \, p(s|\theta) \, p(\theta)}_{p(s)} \qquad \text{Var}(S)(\lambda) = \mathbb{E}[(S - \bar{S})^2] = \int_S ds \, (s - \bar{S})^2 \underbrace{\int_\theta d\theta \, p(s|\theta) \, p(\theta)}_{p(s)}$$

$$p(s) = \int_0^1 \int_0^1 \int_0^1 \int_{\mathbb{R}} \int_{\mathbb{R}} d\theta \; p(s|\theta) \; \frac{1}{\sqrt{2 \pi \Sigma_{\mu_a}}} \exp^{-\frac{(\theta_4 - \bar{\mu_a}^{\text{HHb}}(\lambda))^2}{2 \Sigma_{\mu_a}}} \frac{1}{\sqrt{2 \pi \Sigma_{\mu_a}}} \exp^{-\frac{(\theta_5 - \bar{\mu_a}^{\text{HbO2}}(\lambda))^2}{2 \Sigma_{\mu_a}}}$$

$$= \int_0^1 \int_0^1 \int_0^1 \int_{\mathbb{R}} \int_{\mathbb{R}} d\theta \; \frac{1}{\sqrt{2 \pi \Sigma_s}} \exp^{-\frac{(s - \Gamma \mu_a(\theta) \varphi_t(\theta))^2}{2 \Sigma_s}} \frac{1}{2 \pi \Sigma_{\mu_a}} \exp^{-\frac{(\theta_4 - \bar{\mu_a}^{\text{HHb}}(\lambda))^2 + (\theta_5 - \bar{\mu_a}^{\text{HbO2}}(\lambda))^2}{2 \Sigma_{\mu_a}}}$$
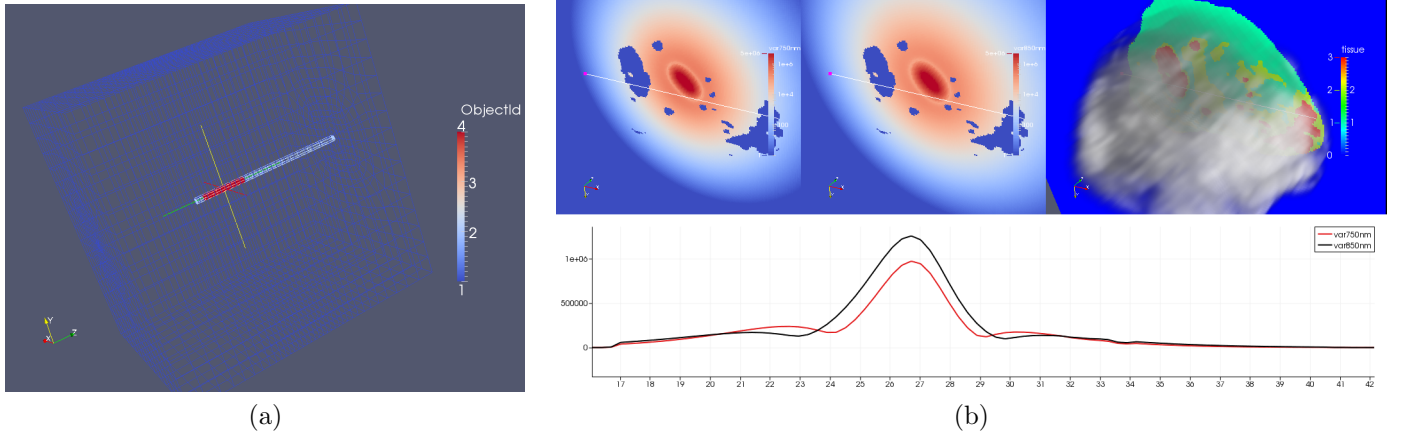

(a)

(b)

Figure 2: Wavelength Sensitivity. (a) The model of the laser applicator is registered to the prostate data set shown in Figure 1. (b) The predicted sensitivity at $\lambda = 750nm$ and $\lambda = 850nm$ is shown. As expected the photoacoustic source is most sensitive, ie provides the most information near the laser fiber. Line profiles quantitatively compare the expected sensitivity with distance from the laser fiber as well as variations over distinct tissue types.

References

[Ahmed and Gokhale, 1989] Ahmed, N. A. and Gokhale, D. (1989). Entropy expressions and their estimators for multivariate distributions. *IEEE Transactions on Information Theory*, 35(3):688–692.

[Carp et al., 2004] Carp, S. A., Prahl, S. a., and Venugopalan, V. (2004). Radiative transport in the delta-P1 approximation: accuracy of fluence rate and optical penetration depth predictions in turbid semi-infinite media. *Journal of biomedical optics*, 9(3):632–47.

[Duck, 1990] Duck, F. (1990). Physical properties of tissue: a comprehensive reference book. *London, UK: Academic.*

[Durrett, 2010] Durrett, R. (2010). *Probability: theory and examples.* Cambridge university press.

[Fahrenholtz et al., 2015] Fahrenholtz, S., Moon, T., Franco, M., Medina, D., Hazle, J. D., Stafford, R. J., Maier, F., Danish, S., Gowda, A., Shetty, A., Warburton, T., and Fuentes, D. (2015). A Model Evaluation Study for Treatment Planning of Laser Induced Thermal Therapy. *International Journal of Hyperthermia.* in preparation.

[Fahrenholtz et al., 2013] Fahrenholtz, S., Stafford, R. J., Hazle, J., and Fuentes, D. (2013). Generalised polynomial chaos-based uncertainty quantification for planning MRgLITT procedures. *International Journal of Hyperthermia*, 29(4):324–335. PMC3924420.

[Fasano et al., 2010] Fasano, A., Hömberg, D., and Naumov, D. (2010). On a mathematical model for laser-induced thermotherapy. *Applied Mathematical Modelling*, 34(12):3831–3840.

[Fuentes et al., 2013] Fuentes, D., Elliott, A., Weinberg, J. S., Shetty, A., Hazle, J. D., and Stafford, R. J. (2013). An Inverse Problem Approach to Recovery of In-Vivo Nanoparticle Concentrations from Thermal Image Monitoring of MR-Guided Laser Induced Thermal Therapy. *Ann. BME.*, 41(1):100–111. PMC3524364.

[Fuentes et al., 2010] Fuentes, D., Feng, Y., Elliott, A., Shetty, A., McNichols, R. J., Oden, J. T., and Stafford, R. J. (2010). Adaptive Real-Time Bioheat Transfer Models for Computer Driven MR-guided Laser Induced Thermal Therapy. *IEEE Trans. Biomed. Eng.*, 57(5). Cover Page, PMC3857613.

[Fuentes et al., 2009] Fuentes, D., Oden, J. T., Diller, K. R., Hazle, J., Elliott, A., , Shetty, A., and Stafford, R. J. (2009). Computational Modeling and Real-Time Control of Patient-Specific Laser Treatment Cancer. *Ann. BME.*, 37(4):763. PMC4064943.

[Fuentes et al., 2011] Fuentes, D., Walker, C., Elliott, A., Shetty, A., Hazle, J., and Stafford, R. J. (2011). MR Temperature Imaging Validation of a Bioheat Transfer Model for LITT. *International Journal of Hyperthermia*, 27(5):453–464. Cover Page, PMC3930085.

[MacLellan et al., 2013] MacLellan, C. J., Fuentes, D., Elliott, A. M., Schwartz, J., Hazle, J. D., and Stafford, R. J. (2013). Estimating nanoparticle optical absorption with magnetic resonance temperature imaging and bioheat transfer simulation. *International Journal of Hyperthermia*, (0):1–9.

[Madankan et al., 2015] Madankan, R., Stefan, W., Hazle, J. D., Stafford, R. J., and Fuentes, D. (2015). Accelerated Model-based Signal Reconstruction for Magnetic Resonance Imaging in Presence of Uncertainties. *IEEE Trans. Med. Img.* submitted.

[Modest, 2013] Modest, M. F. (2013). *Radiative heat transfer*. Academic press.

[Stefan et al., 2015] Stefan, W., Fuentes, D., Yeniaras, E., Hwang, K., Hazle, J. D., and Stafford, R. J. (2015). Novel Method for Background Phase Removal on MRI Proton Resonance Frequency Measurements. *Trans. Medical Imaging.* in review.

[Welch, 1984] Welch, A. J. (1984). The thermal response of laser irradiated tissue. *Quantum Electronics, IEEE Journal of*, 20(12):1471–1481.

[Welch and Van Gemert, 1995] Welch, A. J. and Van Gemert, M. J. (1995). *Optical-thermal response of laser-irradiated tissue*, volume 1. Springer.

[Yung et al., 2015] Yung, J., Fuentes, D., MacLellan, C. J., Maier, F., Hazle, J. D., and Stafford, R. J. (2015). Referenceless Magnetic Resonance Temperature Imaging using Gaussian Process Modeling. *Medical Physics.* in review.
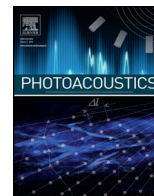
Research Article

Photoacoustic imaging driven by an interstitial irradiation source

Q1 Trevor Mitcham [a,c], Katherine Dextraze [a,c], Houra Taghavi [a], Marites Melancon [b,c], Richard Bouchard [a,c]

[a] Department of Imaging Physics, University of Texas MD Anderson Cancer Center, Houston, TX 77030, USA
[b] Department of Interventional Radiology, University of Texas MD Anderson Cancer Center, Houston, TX 77030, USA
[c] Graduate School of Biomedical Sciences, University of Texas at Houston, Houston, TX 77030, USA

ABSTRACT

Photoacoustic (PA) imaging has shown tremendous promise in providing valuable diagnostic and therapy-monitoring information in select clinical procedures. Many of these pursued applications, however, have been relatively superficial due to difficulties with delivering light deep into tissue. To address this limitation, this work investigates generating a PA image using an interstitial irradiation source with a clinical ultrasound (US) system, which was shown to yield improved PA signal quality at distances beyond 13 mm and to provide improved spectral fidelity. Additionally, interstitially driven multi-wavelength PA imaging was able to provide accurate spectra of gold nanoshells and deoxyhemoglobin in excised prostate and liver tissue, respectively, and allowed for clear visualization of a wire at 7 cm in excised liver. This work demonstrates the potential of using a local irradiation source to extend the depth capabilities of future PA imaging techniques for minimally invasive interventional radiology procedures.

© 2015 The Authors. Published by Elsevier GmbH. This is an open access article under the CC BY-NC-ND license (http://creativecommons.org/licenses/by-nc-nd/4.0/).

1. Introduction

In the past twenty years, image guidance has been utilized increasingly to improve the precision and efficacy of diagnostic and therapeutic procedures [1]. Typically, image guidance is provided by ultrasound (US), X-ray computed tomography, fluoroscopy, or magnetic resonance imaging. Photoacoustic (PA) imaging is a promising technique that is non-ionizing, low-cost, and offers high-contrast imaging of both the surgical tools and photoabsorbers that are often encountered in diagnostic and therapeutic techniques. To provide accurate guidance, PA images can be co-registered with US imaging to generate a photoacoustic-ultrasonic (PAUS) image that contains clear anatomical information and provides high-contrast visualization of important photoabsorbers, such as hemoglobin or targeted nanoparticles [2]. To date, however, the application of PAUS imaging has typically been limited to superficial anatomical sites due to the relatively shallow penetration depth of the external irradiation source.

PA imaging requires a narrow-pulse-width laser irradiation source, photoabsorbers to generate PA-induced pressure waves, and an US transducer for signal detection. The light provided by the pulsed irradiation source is absorbed by photoabsorbers and immediately converted to heat. This thermal transient leads to rapid local expansion, creating pressure waves that can be detected with high spatiotemporal resolution by an US transducer. The resulting pressure waves are dependent on local fluence, optical absorption, and thermally dependent material properties [3]. The initial local pressure (p_0) generated by the PA effect can be described as

$$p_o = \frac{\beta c^2}{C_p}\mu_a F = \Gamma A, \tag{1}$$

where $\beta[\frac{1}{K}]$ is the thermal coefficient of volume expansion, $c[\frac{m}{s}]$ is the speed of sound through tissue, $C_p[\frac{J}{K \cdot kg}]$ is the heat capacity at constant pressure, $\mu_a[\frac{1}{cm}]$ is the optical absorption coefficient, $F[\frac{J}{cm^2}]$ is the local laser fluence, Γ is the Grüneisen coefficient, and $A[\frac{J}{cm^3}]$ is the local deposition energy.

As laser light travels through a medium (e.g., tissue), fluence is lost due to optical scattering and absorption by tissue components like blood and adipose tissue. This fluence loss is the primary cause of the limited depth penetration that has previously hindered the clinical application of PA imaging. Compensating for fluence loss is a nuanced problem. The laser fluence applied to skin in clinical applications is regulated by the American National Standards Institute (ANSI), which recommends that clinical skin exposure to low near-infrared (NIR) light not exceed specific fluence levels

E-mail address: rrbouchard@mdanderson.org.

ranging from 20 $\frac{mJ}{cm^2}$ at 700 nm, to 50 $\frac{mJ}{cm^2}$ at 900 nm, to 100 $\frac{mJ}{cm^2}$ at 1050 nm [4,5]. Therefore, depth penetration cannot be improved by simply increasing surface fluence. Previous work has explored using a 1064-nm wavelength laser for PA imaging applications. At this wavelength, tissue scattering and absorption is decreased compared to lower NIR wavelengths, while the exposure limitations through skin rise linearly to 100 $\frac{mJ}{cm^2}$, providing a situation in which more laser light can be delivered to target photoabsorbers [4–6]. The reduction in tissue scattering and absorption at 1064 nm also results in reduced background signal in PA images, which improves the contrast of the images compared to imaging at lower wavelengths in the NIR range [7]. However, the depth penetration with 1064-nm irradiation can still be quite limited for clinical applications, and such an implementation can restrict opportunities for multi-wavelength imaging. One final method to improve imaging depth is to fundamentally change the absorption properties of the target being imaged, a technique that has been demonstrated for metallic objects [8].

To circumvent the depth penetration limitation of NIR irradiation, endoscopic, intravascular and transrectal PA imaging techniques have been developed for targeting deeper tissues [9–14]. Although these techniques have been effective for imaging particular structures, such as the prostate, colon, or vascular wall, they have not been applied more generally to deep-tissue imaging. Furthermore, the smaller US transducers that are used to accommodate PA endoscopic or intravascular imaging have lower sensitivity and a reduced receive-aperture extent (compared to larger, more conventional US arrays), resulting in reduced image quality [15]. Therefore, in order to deliver light to deep tissues while maintaining image quality, an interstitial optical source could be introduced to provide local irradiation of the target while a conventional diagnostic US array could be used for external acoustic detection and PA image formation.

This work investigated the use of a single interstitial optical fiber co-registered with an external US transducer to provide PA images for specific interventional radiology (IR) procedures (e.g., laser ablation or biopsy guidance). Optical fibers were modified to serve as a local, interstitial irradiation source. To demonstrate initial feasibility of the interstitial PA imaging system, wire targets, gold nanoshells (AuNSs), and deoxyhemoglobin were imaged in tissue-mimicking phantoms and in ex-vivo tissue.

2. Materials and methods

2.1. General setup and fiber processing

The imaging setup consisted of a pulsed laser source that triggered the receive acquisition of a clinical US system. A Quanta-Ray® PRO pulsed Nd:YAG laser coupled into a tunable GWU versaScan optical parametric oscillator (OPO; Newport Corp., Irvine, CA) was used to provide pulsed NIR irradiation. After exiting the OPO, the beam was sent through a neutral-density filter to a plano-convex focusing lens (Thorlabs Inc., Newton, NJ) that adjusted the spot size to allow for better coupling into optical fibers with a 1000-μm diameter. This diameter was chosen because it coincides with the size of needles often used in biopsy procedures, providing more clinically relevant implantation of the fiber into the tested phantoms [16]. After the focusing lens, a custom-built fiber holder was connected to a three-dimensional micrometer-driven platform to allow for precision translation of the fiber coupling stage (MBT616D; Thorlabs Inc., Newton, NJ). From the coupling stage, the fiber was inserted into a phantom and used to generate a PA signal that was detected with a Vantage 128 US system using an L11-4v linear array operating at 6.25 MHz (Verasonics, Inc., Redmond, WA). A schematic of the complete
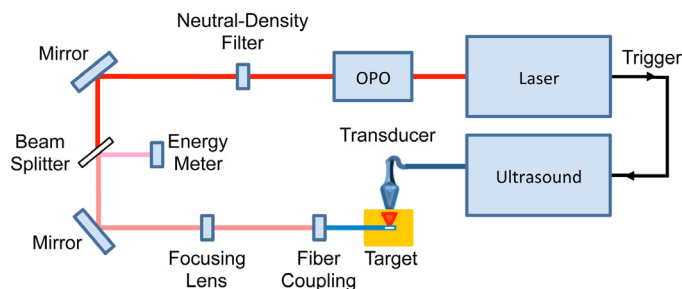

**Fig. 1.** Schematic of PA imaging system driven by an interstitial irradiation source.

system setup is provided in Fig. 1. Pulse energy readings were taken with a Nova II meter connected to a PE50-DIF-ER-V2 detector with diffuser (Ophir Optronics Solutions Ltd., Jerusalem, Israel) while laser wavelength was calibrated using a Thorlabs CCS175 compact spectrometer (Thorlabs Inc., Newton, NJ). Energy delivery to the fiber was estimated by splitting the primary beam into the energy meter using a glass slide. The energy meter was also placed at the irradiating side of each fiber prior to a study to determine the wavelength-dependent ratio between measured input energy and output energy. This ratio and the estimated input energy values obtained from the beam splitter were utilized to normalize for output fluence differences between wavelengths. Additionally, laser spot size measurements were taken by coupling a continuous wave (CW) laser into the fiber and measuring the projected spot at 5 mm from the fiber tip.

Two different types of 1000-μm-diameter fibers were used in this study. All but one study utilized custom-built, side-fire 1000-μm fibers (Fig. 2.d; Thorlabs Inc., Newton, NJ). In order for optical fibers to transmit light efficiently, both the proximal (i.e., the end coupled to the incoming laser beam) and distal (i.e., the end acting as a local optical source) ends of the fiber must be beveled to appropriate angles and minimized of surface imperfections [12]. Proximal ends were left flat, polished, then qualitatively inspected using a digital microscope (zipScope; Aven Inc., Ann Arbor, MI,) to ensure surface smoothness (Fig. 2.b-c). If any scratches or cloudy areas were present, the polishing sequence was repeated until the surface appeared visually smooth. Upon completion of the proximal fiber tip, the distal tip was sanded using a custom-built, angled sanding apparatus (Fig. 2.a) until the tip was beveled to a critical angle of 35°; it was then polished in a similar fashion to the procedure implemented for the proximal tip. The distal tip was beveled to promote total internal reflection, which allows the fiber to emit light perpendicularly (i.e., side-fire) rather than out the tip (i.e., straight-fire) [12]. As the coupling medium at the end of the fiber determines the critical angle needed, quartz end-caps were added (Sutter Instrument Co., Novato, CA) to ensure that the fiber tip was always air-backed. The spot size 5 mm lateral from the tip was measured to be approximately 0.2 cm^2. Side-fire fibers were implemented in the majority of the studies as they could be readily produced in-house and they tended to provide increased fluence in their limited irradiation volume.

The last study utilized a clinically-approved fiber with a conical distal tip that provided 360° irradiation from a 35° half angle at the distal tip with a spot size of 2.5 cm^2 (i.e., 3.1 cm circumference and 0.8 cm height) at a lateral distance of 5 mm (Fig. 2.e; Pioneer Optics Co., Bloomfield, CT); this fiber is typically used for administration of photodynamic therapy.

All tissue-mimicking phantoms used in this investigation were created using 8% (wt%) gelatin (Sigma-Aldrich Co., St. Louis, MO), 5% Intralipid® (Sigma-Aldrich, St. Louis, MO), 1% silica (US Silica, Frederick, MD), 0.1% formaldehyde (Sigma-Aldrich Corp., St. Louis, MO), and 85.9% deionized (DI) H$_2$O in order to generally mimic the
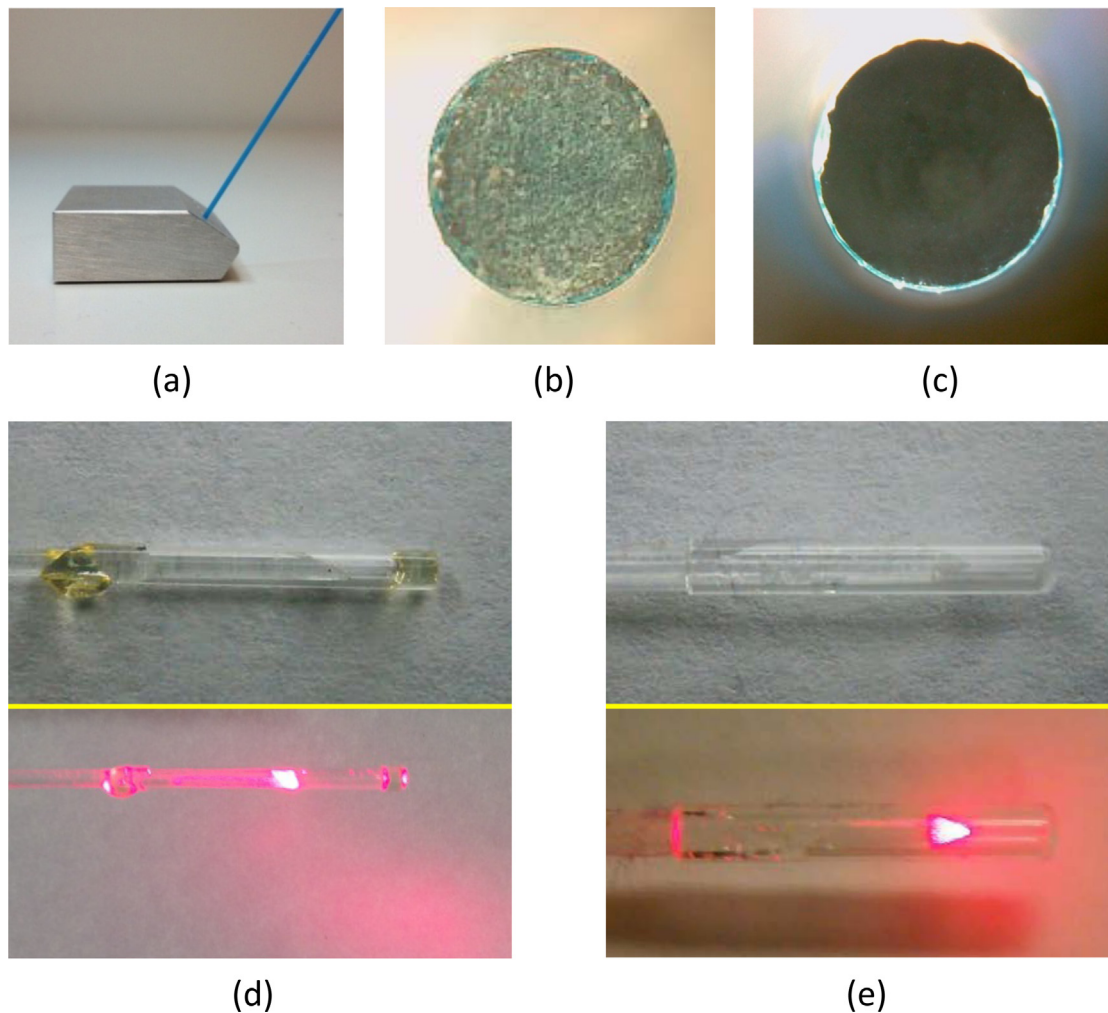
Fig. 2. Optical fiber polishing block, stages of fiber preparation, and completed fiber tips and CW irradiation patterns. (a) Beveled fiber block allows for creation of 35° angle on distal fiber tip for light deflection. (b) Magnified image of proximal fiber tip before sanding or polishing. (c) Magnified fiber tip after polishing with 5-μm polishing film. (d) Magnified capped side-fire fiber tip (top) and CW irradiation pattern (bottom). (e) Magnified capped conical-tip fiber (top) and CW irradiation pattern (bottom).

acoustic and optical properties of tissue [17]. For all studies using interstitial irradiation, the fiber source was placed approximately 5 mm laterally from the imaging target, while PA-induced acoustic signal generation was detected with an external linear US transducer. Pulse-echo US was then used to align the imaging plane with the target of interest. All data presented were normalized for wavelength-dependent differences in surface/fiber fluence. Quantitative analysis of PA data was achieved by selecting a region of interest (ROI) that included only the desired photoabsorber (e.g., titanium wire). In all plots with error bars, the average and standard deviation for each point is presented; the specific sample number for each plot is provided in the figure caption.

2.2. Tissue-mimicking depth phantom

To demonstrate the improvement in depth penetration when using interstitial irradiation, the first study imaged wires at increasing depth within a tissue-mimicking phantom using both interstitial and conventional (i.e., external) laser irradiation. Due to the geometry of the laser setup (Fig. 1), conventional irradiation had to occur from the side while the US probe was placed on top of the phantom. Wire targets were placed in the phantom along a diagonal line with increasing depth. Given this construction, the distance traveled by the photons (d_p) was approximately equal to the acoustic propagation distance (d_a) to the transducer (Fig. 3.a). Wires were included at 7, 20, 37, and 47 mm depths (d_a) with corresponding

lateral offsets (d_p) of 13, 23, 35, and 46 mm. Note that the first wire was displaced more laterally than initially desired to allow for adequate transducer positioning at the edge of the phantom. Using conventional irradiation, 35-40 mJ of energy at 800 nm entered the surface of the phantom (approximately 0.8 cm^2 spot size). In comparison, when using interstitial irradiation, pulse energy was only 6 mJ at 720 nm (i.e., 30 $\frac{mJ}{cm^2}$ at 5 mm) and had a maximum energy of 8 mJ at 900 nm (i.e., 40 $\frac{mJ}{cm^2}$ at 5 mm). Signal-to-noise ratio (SNR) and contrast-to-noise ratio (CNR) were calculated as [18,19]

$$\mathrm{SNR} = \frac{\overline{S_i}}{\sigma_o}, \mathrm{CNR} = \frac{\overline{S_i} - \overline{S_o}}{\sqrt{\sigma_i^2 + \sigma_o^2}}, \tag{2}$$

where $\overline{S_i}$ and $\overline{S_o}$ are the mean signals inside and outside of the target, respectively, and σ_i and σ_o are signal standard deviations of these inside and outside regions, respectively. The ROI was 2 mm (axial) x 12 mm (lateral) and was assigned based on the US B-mode image. The noise (i.e., outside) kernel was of equal size and 1.5 mm above each wire target. This ROI remained fixed for all trials within each study.

2.3. Spectral-fidelity phantom

A tissue-mimicking phantom with an AuNS inclusion was fabricated to assess the effect of depth-dependent scattering on
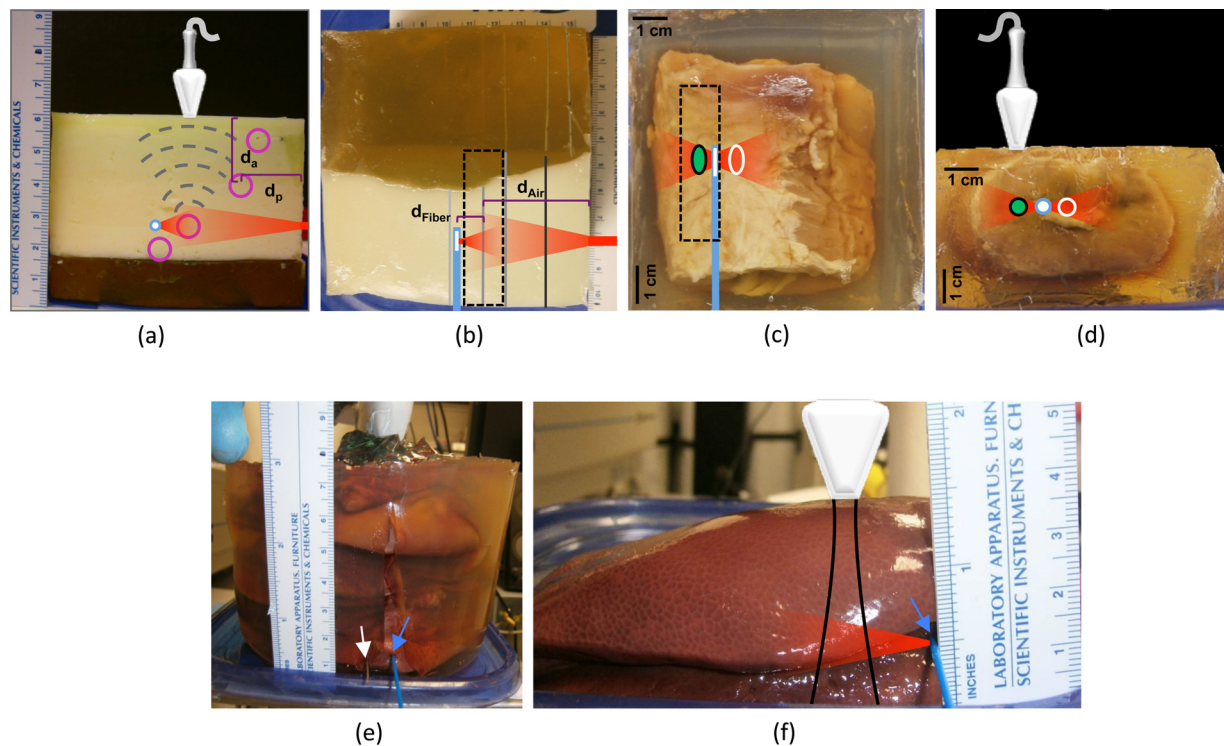
Fig. 3. (a) Side-view of tissue-mimicking phantom with wire inclusions and short-axis outline of transducer provided overhead; purple circles represent location of wires, while blue-white circle denotes location of interstitial fiber; dashed gray lines depict propagation of acoustic waves; external and interstitial irradiation volumes are denoted in red; d_p is distance traveled by photons for external irradiation, while d_a is distance traveled by acoustic wave for both irradiation types. (b) Top-view of phantom; transducer footprint is depicted by black dashed line; blue line represents side-fire imaging fiber location. (c) Top-view of prostate sample; green ellipse represents area of AuNS injection, while white ellipse denotes control region. (d) Side-view of prostate sample. (e) Stack of liver sections cast in pure gelatin for deep interstitial laser delivery; irradiation fiber (blue arrow) and wire imaging target (white arrow) are visible at bottom of image. (f) Liver sample for PA spectroscopy by interstitial laser irradiation; black lines indicate approximate US imaging volume.

214 multi-wavelength imaging. The AuNS target was multi-spectrally
215 imaged (720, 740, 745, 750, 755, 760, 765, 770, 775, 780, 800, 825,
216 850, & 900 nm) with both external irradiation (1.7 cm depth from
217 the incident surface and 35-40 mJ with a 0.8 cm^2 spot size) and
218 interstitial irradiation (6-8 mJ per pulse). All nanoparticle
219 experiments used AuroShell® gold nanoshells (Nanospectra
220 Biosciences, Inc., Houston, TX) that had an optical absorption
221 peak at 760 nm (Fig. 6.c). Absorption profiles were obtained on the
222 AuNS particles using a Synergy™ HT multi-mode microplate reader
223 (BioTek Instruments, Inc., Winooski, VT). For statistical analysis, a
224 4 mm (axial) x 15 mm (lateral) kernel was utilized.

225 *2.4. Prostate tissue phantom*

226 To demonstrate feasibility of imaging with interstitial irradia-
227 tion in tissue, the next study in this investigation involved imaging
228 nanoparticle inclusions in ex-vivo bovine prostate tissue (Animal
229 Technologies Inc., Tyler, TX), where the nanoparticle clusters
230 modeled clinical regions of interest such as ablation targets. The
231 prostate tissue was trimmed of all loose fat and abnormalities and
232 then cast in a pure gelatin phantom (8% gelatin; 92% DI H$_2$O). One
233 site at a depth of approximately 15 mm from the proximal prostate
234 surface was chosen for injection with AuNS particles. In order to
235 prevent migration within the prostate tissue, the particles were
236 suspended in 8% gelatin (1:1 volume ratio) before injection. After
237 injecting the prostate tissue with the particles, the phantom
238 solidified at 4°C for 2 hours. The resulting phantom is shown in
239 Fig. 3.c-d. An 18-gauge needle was used to create a path in the
240 tissue for introduction of the optical fiber approximately 5 mm
241 medial to the inclusions and at equal depth. Images were
242 generated in the region containing nanoparticles as well as in
243 an adjacent control region (i.e., no particles). The targets were

244 imaged multi-spectrally (same wavelengths used in 2.3) using
245 interstitial irradiation with pulse energies ranging from 6-8 mJ.
246 Data analysis was achieved with a 4 mm (axial) x 6 mm (lateral)
247 kernel about each ROI.

248 *2.5. Liver tissue phantom*

249 *2.5.1. Wire imaging*
250 The next study focused on imaging a titanium wire in ex-vivo
251 liver tissue to assess imaging depth in highly absorbing tissue. Ex-
252 vivo porcine liver samples (Animal Technologies Inc., Tyler, TX)
253 were stacked 7.5 cm high and encased in gelatin to prevent
254 movement (Fig. 3.e). A wire target was inserted into the tissue at
255 7 cm depth from the transducer face; note that the transducer long
256 axis was orientated slightly oblique to the wire. An interstitial
257 irradiation source was then inserted at an equal depth to the wire,
258 5 mm away laterally, and used to produce a PA signal from the
259 wire. All images were generated using 800 nm irradiation with
260 8 mJ of energy per pulse.

261 *2.5.2. Deoxyhemoglobin imaging*
262 To demonstrate the multi-wavelength imaging capabilities of
263 interstitial PA imaging and to assess spectral fidelity of an
264 endogenous absorber, ex-vivo liver tissue was multi-spectrally
265 imaged (720, 740, 745, 750, 755, 760, 765, 770, 775, 800, 825, &
266 850 nm) using only interstitial irradiation (6-8 mJ of energy at the
267 fiber tip) at a depth of 1.6 cm from the transducer. Image analysis
268 kernels (4 mm axial x 4 mm lateral) were centered on points
269 5.8 mm, 8.1 mm, and 10.4 mm lateral from the distal fiber tip and
270 analyzed to assess the degree of spectral shift (Fig. 7b). PA spectra
271 were compared to the known deoxyhemoglobin absorption
272 spectrum.

2.6. Conical-tip fiber

In an effort to demonstrate the potential of irradiating larger portions of tissue with an interstitial source, the next study imaged wire targets using a clinically-approved optical fiber with a conical termination that provides 360° irradiation about the distal tip (Fig. 2.e and Fig. 8.b). Two wire targets were embedded in gelatin at equal depth, and the optical fiber was inserted between the two, equidistant from each wire. The wires were imaged with the conical-tip fiber (2.5 mJ at 760 nm) at 3 different orientations (i.e., 0°, 90°, 180°) and compared to images generated with a custom-built, side-fire fiber (7 mJ at 760 nm), which only illuminated a sector of the surrounding volume (Fig. 8.a). Note that energy irradiating from the conical-tip fiber was only measured in one direction with the energy meter previously described. For data analysis purposes, a 2 mm (axial) x 2 mm (lateral) kernel was used.

2.7. Fiber-tip artifact

In all trials, the space immediately surrounding the fiber tip was obscured by a PA-signal artifact of unknown origin (white arrows in Fig. 8). In order to attempt to better understand and assess the source of this artifact (i.e., phantom-dependent or fiber-dependent), fiber tips of different varieties were imaged in pure gelatin as well as an absorbing/scattering tissue-mimicking phantom free of all targets. The tissue-mimicking phantom was created using the recipe previously provided with the addition of 0.01% black ink (Dromgooles Fine Writing Instruments, Houston, TX) to provide an optical density of 1. Beveled and capped fibers, unbeveled and capped fibers, and unbeveled and uncapped fibers were imaged at the fiber tip in both phantom types with contrast values recorded for each. Imaging was performed with 8 mJ of energy at 800 nm, while a 4 mm (axial) x 6 mm (lateral) kernel was used for data analysis.
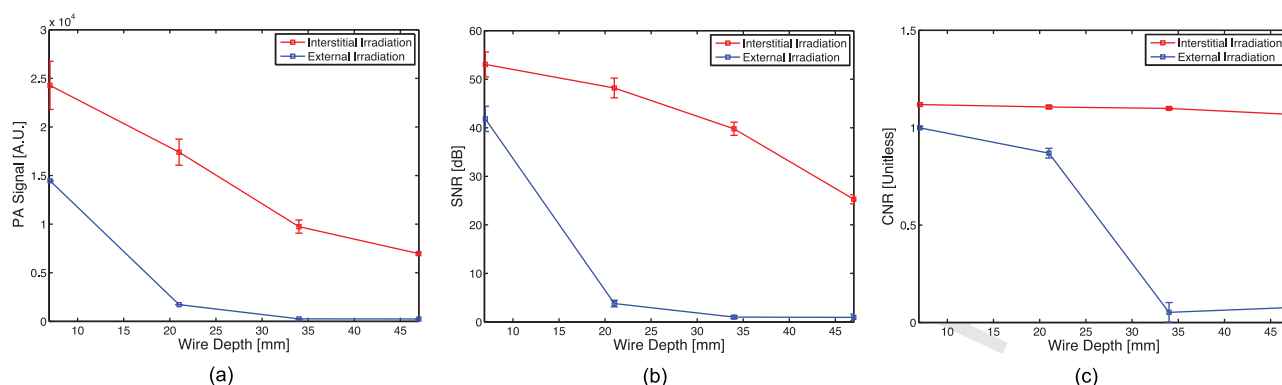
3. Results

3.1. Tissue-mimicking depth phantom

Results from the tissue-mimicking depth phantom study demonstrate that interstitial irradiation, using significantly less energy, can provide better image quality than external irradiation at photon propagation distances of 13 mm or greater. As seen in Fig. 4, when the dynamic range is kept constant throughout each trial, PA signal from the wire target can be clearly seen at greater depths using interstitial irradiation (i.e., 37, 47 mm), while it is not visible with external irradiation for the same depth range. Some artifacts are present in the images due to reverberation in the wire target and a near-field artifact resulting from transducer crosstalk. Additionally, as shown in Fig. 5.a, the SNR resulting from external irradiation decreases from 41.8 at 7 mm depth to 0.95 at 47 mm in depth, while the SNR resulting from interstitial irradiation ranges from 53.1 to 25.3 over the same depth span. In a similar fashion (Fig. 5.b), the CNR resulting from external irradiation decreases from 0.99 to 0.07 over the course of increased imaging depth, while the CNR resulting from interstitial irradiation only decreases from 1.12 to 1.07.
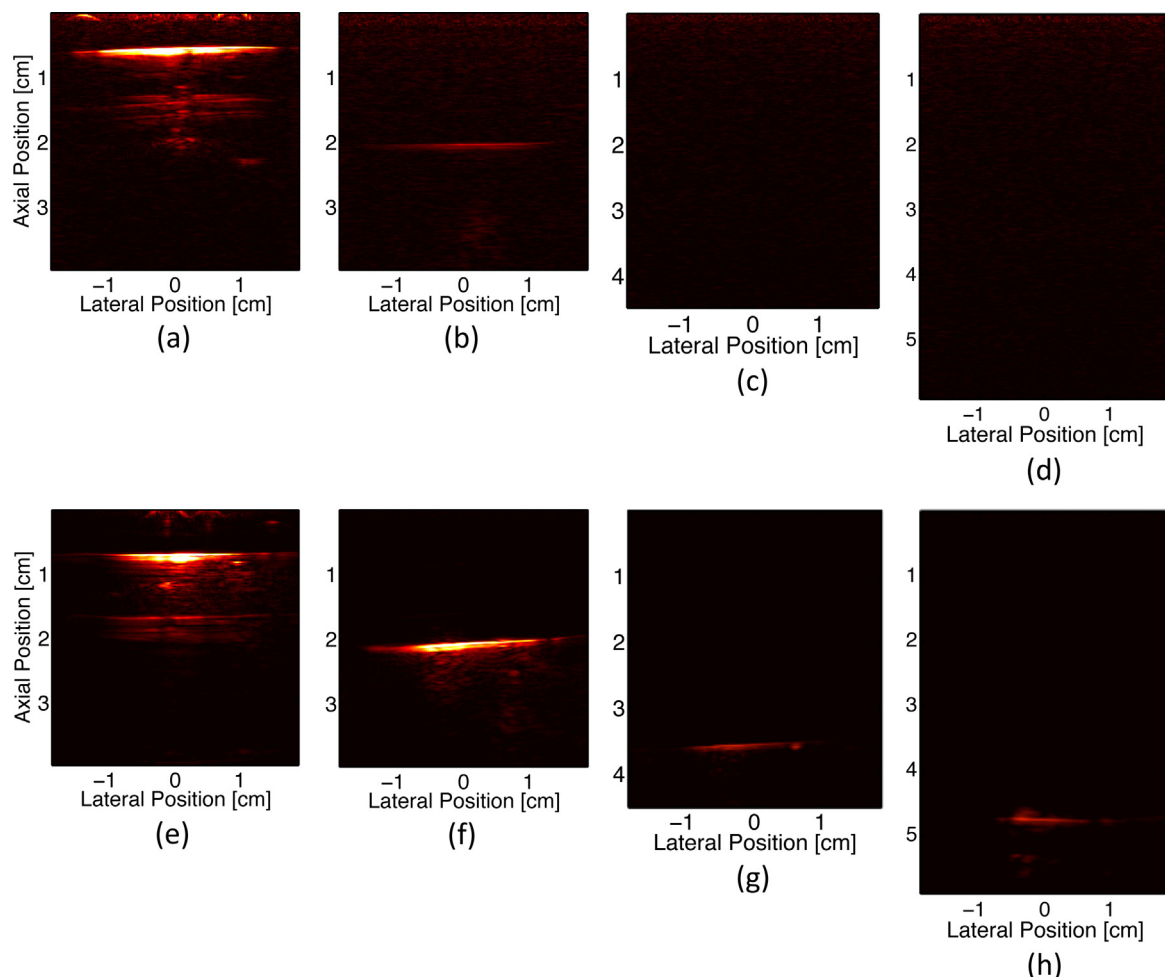
Fig. 4. PA images of wire at different depths (7, 20, 37, & 47 mm depths) in a tissue-mimicking phantom. (a) - (d) PA imaging driven by external irradiation; (e) - (h) PA imaging driven by interstitial irradiation. Note dynamic range is kept constant for all images of same irradiation type.

Fig. 5. (a) PA signal, (b) SNR, and (b) CNR plot (N = 10) comparison of PA imaging of wires at increasing depth driven by interstitial (red) or external (blue) irradiation.

3.2. Spectral-fidelity phantom

Results from the spectral fidelity study show that interstitial imaging provides more accurate spectral information than traditional irradiation methods in a tissue-mimicking phantom. The nanoparticles imaged had broadband absorption in the low-NIR range, with an absorption peak at 760 nm. As can be seen in Fig. 6.a, interstitial irradiation provided an absorption spectrum which peaked at 760 nm and generally decreased monotonically away from this peak. Conversely, traditional irradiation methods produced an absorption spectrum which peaked at 800 nm, demonstrating a redshift inherent to traveling through scattering tissue.

3.3. Prostate tissue phantom

Results from the prostate tissue phantom study demonstrate that it is possible to spectroscopically identify specific photo-absorbers using interstitial irradiation in ex-vivo tissue. As shown in Fig. 6.b, the signal from the region containing nanoparticles can clearly be discerned when compared to the control region. The signal from the injection site closely matches the absorption spectrum of the injected nanoparticles (Fig. 6.c), while the signal from the control (i.e., non-injected) site strongly resembles the spectrum of deoxyhemoglobin (Fig. 7.d).

3.4. Liver tissue phantom

3.4.1. Wire imaging

Results from the ex-vivo liver phantom show that PA signals generated 7 cm from the transducer face in a highly absorbing medium using only 8 mJ of energy in the low-NIR range can be readily imaged. Fig. 7.a shows the image of the embedded titanium target generated by interstitial irradiation.

### 3.4.2. Deoxyhemoglobin imaging

Results from the ex-vivo liver imaging study also indicate that endogenous absorbers can be spectroscopically isolated at depth. Approximately two centimeters deep from the transducer face, the spectroscopic PA signal (Fig. 7.b) obtained from the three regions of excised liver tissue correlated very strongly with that of deoxyhemoglobin (Fig. 7.c-d). The imaged signals all have the characteristic deoxyhemoglobin "hump" at approximately 758 nm. However, as distance from the fiber tip increases, spectral fidelity decreases as a red-shift in the spectra occurs. Interstitial irradiation at 5 mm from the fiber tip causes minimal shift in the signal with approximately 1.3 nm of redshift for every mm increase in distance from the fiber tip observed.

3.5. Conical-tip fiber

The results from the conical-tip fiber studies show that 360° irradiation of target tissue, which is not possible with a simple beveled fiber, is achievable through the use of a conical tip. The signal generated by each wire was approximately equal when irradiated with the conical tip, while at most only one wire generated signal when irradiated by the beveled tip, as seen in Fig. 8. Contrast values for the right and left wires using the side-fire fibers were 7.19 (0°) and 9.37 (180°), respectively, when directly irradiated and 2.35 or less when not directly irradiated (e.g., right wire in Fig. 8.e). For the conical-tip fiber, contrast values ranged from 2.07 to 3.47 for all rotation orientations and wires. This fiber removes the directional component introduced
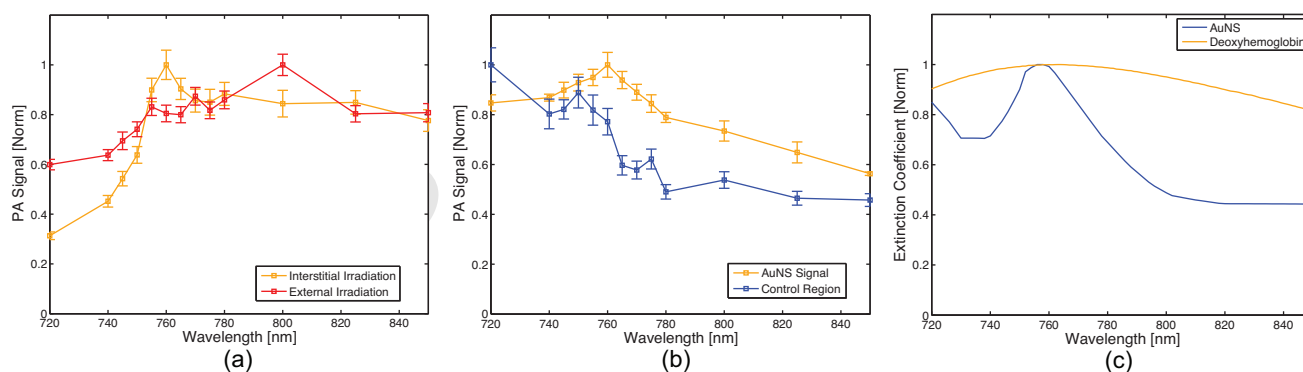
Fig. 6. (a) PA signal spectrum (N = 30) generated by AuNSs in tissue-mimicking phantom using external irradiation (red) with a 17-mm photon propagation distance or interstitial irradiation (gold) with a 5-mm photon propagation distance; (b) PA signal spectrum (N = 30) generated by AuNSs (gold) or deoxyhemoglobin (blue) in ex-vivo prostate tissue using interstitial irradiation; (c) Optical absorption spectrum of AuNSs (gold) and deoxyhemoglobin (blue).
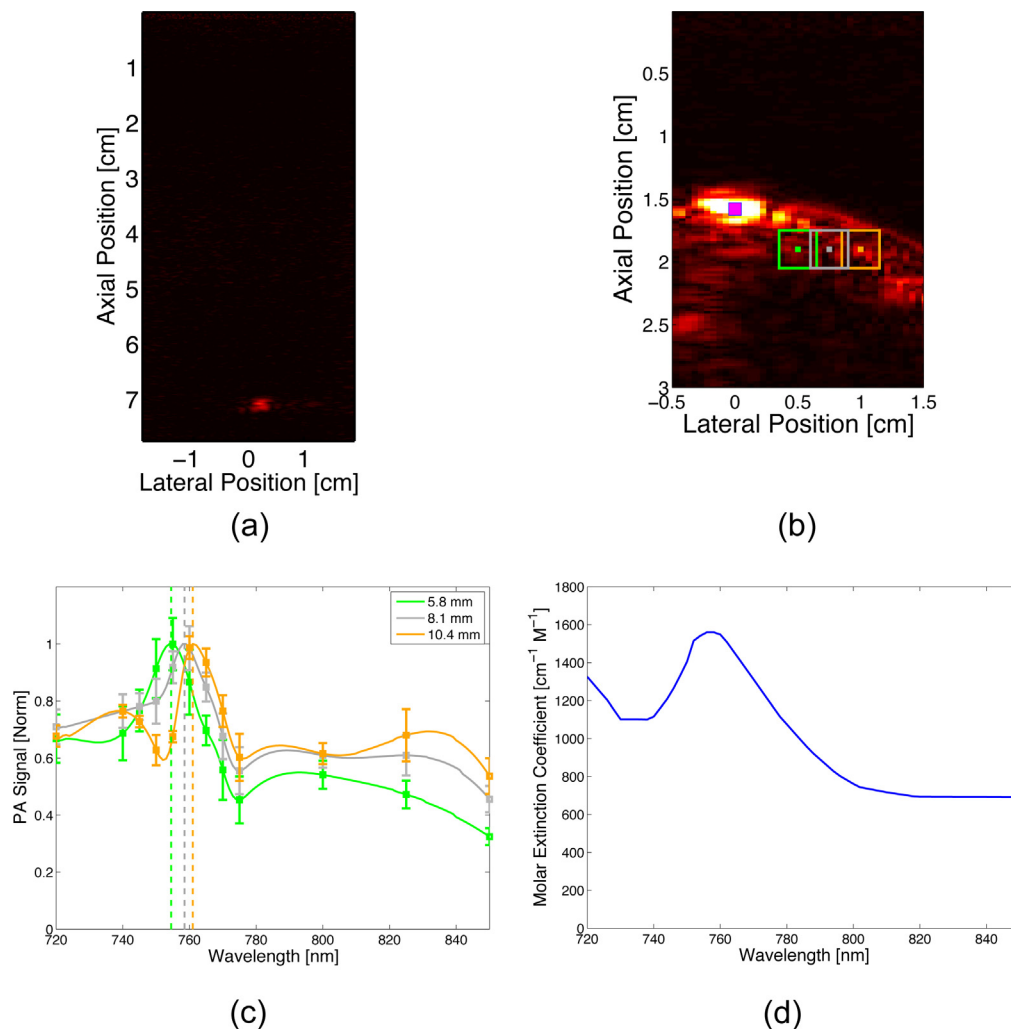
Fig. 7. (a) PA image of wire embedded in ex-vivo liver at 7 cm. (b) PA image of hemoglobin in ex-vivo liver at approximately 2 cm. Magenta spot represents center of fiber, while green, grey, and gold boxes represent kernels for 5.8-mm, 8.1-mm, and 10.4-mm analysis, respectively; dot in center of kernel denotes measurement point (i.e., where distance from the source was measured). (c) Multi-wavelength acquisition (N = 30) of deoxyhemoglobin target at distances of 5.8 mm (green), 8.1 mm (grey), and 10.4 mm (gold) from the inserted fiber tip. (d) Optical absorption spectrum of deoxyhemoglobin [20].

by the beveled fiber tip; although, due to the lower output fluence inherent to this fiber, the overall contrast values are lower. Additionally, this study showed that optical fibers used in the clinic can be repurposed for use in fiber-driven PA imaging.

3.6. Fiber-tip artifact

This study demonstrated that all fiber types in the imaging environments tested generate a PA-signal artifact at their distal tip when imaging. For beveled, straight-capped, and straight-uncapped fibers in gelatin, the contrast values were 27.1 dB, 29.4 dB, and 31.6 dB, respectively, while in an absorbing/scattering tissue-mimicking phantom, the contrast values were 34.7, 40.6, and 36.7, dB, respectively. There was an increase in PA signal for all fiber types when imaging in the tissue-mimicking phantom compared to pure gelatin.

4. Discussion

We have demonstrated that it is feasible to generate a PA image using interstitial irradiation with an external US receive-array. In this study, interstitial irradiation has revealed improved interrogation depth compared to conventional external irradiation. Using an interstitially placed optical fiber, PA images were readily achieved at depths of 7 cm in tissue using only 8 mJ ($40 \frac{mJ}{cm^2}$ at 5 mm), while multi-wavelength imaging was demonstrated 2 cm into tissue. The interstitial irradiation technique investigated maintained better image quality (i.e., SNR, CNR) and spectral fidelity at all depths tested when compared to conventional external irradiation.

Although both beveled-tip and conical-tip fibers were used in this study, potential clinical applications would likely implement an interstitial irradiation fiber with a conical tip in order to achieve a larger irradiation volume (i.e., prostate biopsy). Further modifications to the irradiation fiber may be required for actual clinical application. For instance, a diffuser could be used during 360° irradiation with the conical tip fiber, permitting more of the tissue sample to be imaged at a time and providing a more uniform light distribution [21].

While the fluence levels generated at 5 mm during interstitial irradiation do slightly exceed the acknowledged ANSI limit for skin exposure at some wavelengths (e.g., $30 \frac{mJ}{cm^2}$ at 720 nm versus the 22 $\frac{mJ}{cm^2}$ limit for skin), this fluence would not applied to skin but rather would be inserted directly into soft tissue, which tends to have lower absorption and scattering than skin over the wavelength range used [22,23]. It is also important to note that no tissue damage was noted in any trials using interstitial irradiation, nor were any spectral changes noticed in the tissue samples due to
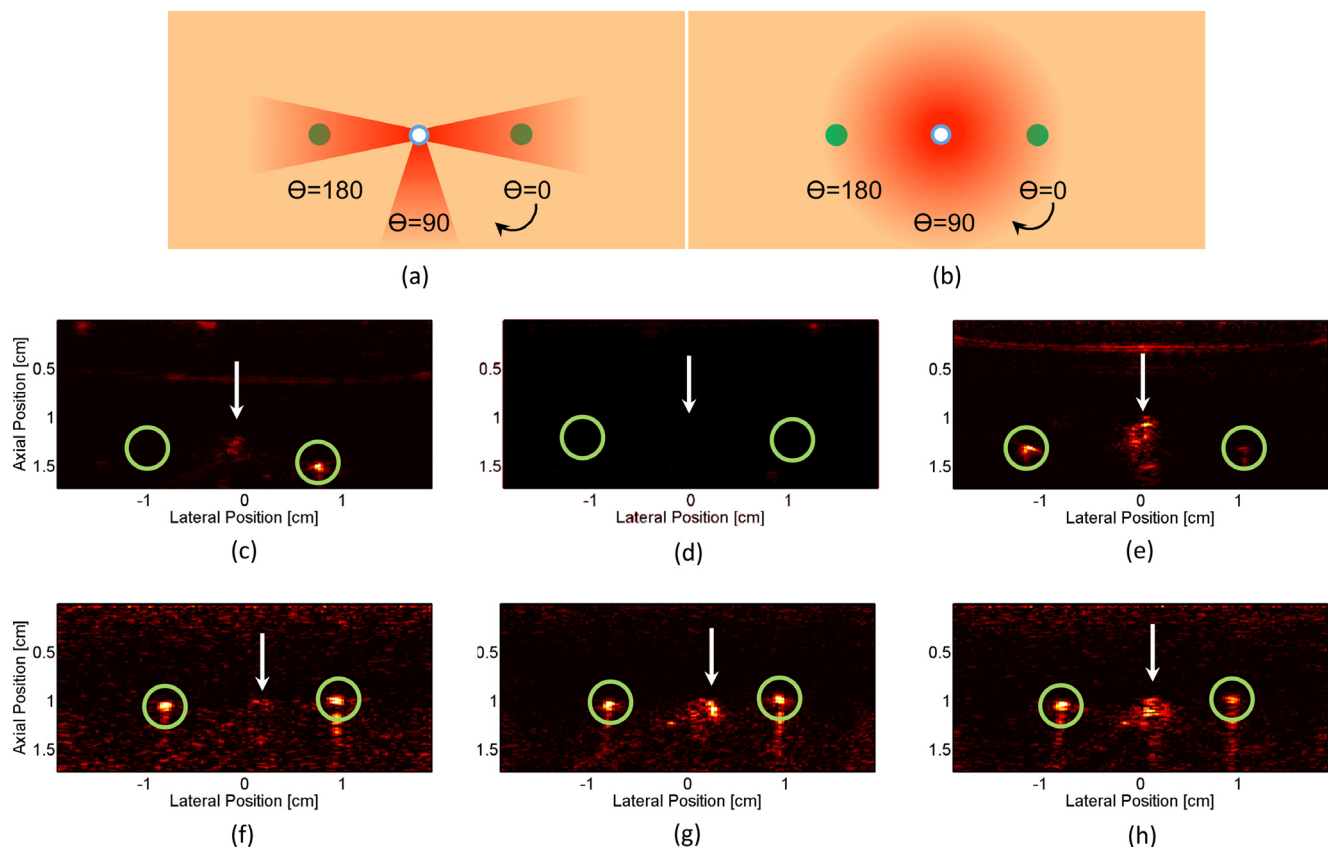
Fig. 8. Side-fire and conical-tip fiber comparison. (a) Illustration of side-fire fiber rotation and irradiation pattern; green circles represent location of wires, while blue-white circle indicates position of fiber tip. (b) Illustration of conical-tip fiber rotation and irradiation pattern. (c) - (h) PA images of two wires embedded in gelatin; white arrows denote PA-signal artifact at fiber location, and green circles outline PA signal generated from wires. PA images generated from side-fire irradiation at (c) 0°, (d) 90°, and (e)180° rotation. (f) PA images generated from conical-tip irradiation at (f) 0°, (g) 90°, and (h) 180° rotation.

ablative processes. Although fluence levels at 5 mm from the distal fiber tip are likely to be safe for clinical use, one concern that must be addressed before clinical adoption is that of high-fluence regions immediately surrounding the fiber tip before the light begins to diffuse. While more research is needed to determine appropriate fluence levels for interstitial irradiation, it is likely that soft tissue can withstand greater fluence levels than skin in the low-NIR range. Should concerns over fluences proximal to the tip be an issue, it could be possible to either increase the diameter of the fiber end-cap and/or add a diffuser (e.g., inflatable balloon tip with a scattering fluid) around the fiber tip to control local fluence levels at the source and thereby protect nearby tissue.

There are instances in the presented results where the PA signal spectra slightly differ from known absorption spectra. One cause for this could be imprecision in wavelength calibration when using the aforementioned spectrometer. Additionally, at lower wavelengths, increased scattering and absorption can cause a decrease in signal beyond what is corrected for by energy normalization, leading to a slight skewing of the data at these wavelengths.

During testing, an artifact appeared in some PA images that was caused from the generation of a PA signal by the irradiating tip of the interstitial fiber. This artifact appeared independent of the imaging medium, occurring in both pure gelatin and tissue-mimicking phantoms. One potential explanation for this artifact is that proximal chromophores adjacent to the fiber tip absorb energy where fluence would be highest (i.e., before tissue scattering occurs). In the case of gelatin phantoms, the water used in the phantom could provide the source of absorption. Despite the low optical absorption of water in the low-NIR range, the relatively high fluence at the fiber tip could be enough to

induce an appreciable PA effect [20]. One further possibility is that mismatched refractive indices at the insertion site (i.e., water-tissue interface immediately surrounding the fiber tip) causes light to backscatter, which could manifest as a fluence gain in the tissue immediately surrounding the fiber tip. Continued classification of the tip artifact will allow for improved imaging using interstitial fibers.

To implement interstitial irradiation, an optical fiber must be introduced percutaneously in order for light to reach the target tissue. Current minimally invasive, standard-of-care techniques common in IR, such as thermal ablations and image-guided biopsies, could reasonably accommodate the optical fiber through placement alongside or following the extraction of interstitial instruments. During photothermal ablation, a fiber delivering the output of a CW laser is already in place within the target tissue [24,25]. To incorporate PA guidance into photothermal therapy, a single optical fiber would remain in place, while the laser source could be switched between the CW source for treatment and the pulsed source required for PA imaging. Radiofrequency (RF) ablation techniques could also be adapted to include an interstitial optical fiber to provide PA imaging to monitor liver and cardiac ablation procedures [26].

PA imaging techniques are also capable of monitoring tissue state during ablative procedures by utilizing thermography and spectroscopy to assess oxygen saturation, tissue denaturation, and temperature [27–29]. In both RF and photothermal ablation techniques, real-time PA-based thermography could be used to monitor the temperature of critical structures adjacent to the ablation target, while assessment of oxygen saturation or tissue denaturation could be used as a treatment endpoint, thereby

providing precise treatment margins [30,31]. However, should clinical fluence value recommendations fall below the values presented, further investigation of the effect of SNR on spectral unmixing in in-vivo animal models will be necessary.

Needle biopsies also provide a practical pathway for interstitial irradiation. During biopsies, real-time PA spectroscopy could be applied for identification of normoxic and hypoxic tissue. Hypoxic or necrotic tissue is characteristic of the core of a fast-growing, possibly aggressive tumor, therefore the clinician could adapt the sampling locations based on the tissue's oxygen state, which could later also be used to inform radiation treatment planning [32]. A typical biopsy needle has a diameter of at least 1.27 mm (18-gauge), which could easily accommodate the 1000-μm optical fibers implemented in this preliminary investigation.

By utilizing B-mode images from the existing US array in concert with interstitial PA imaging, the interstitial irradiation source would be co-registered with the imaging plane, while the B-mode images would provide anatomical visualization and context of surrounding tissue structures during a clinical procedure [2]. Photoacoustic imaging driven by an interstitial irradiation source, especially if combined with the proven anatomical visualization capabilities of B-mode imaging, shows great promise for IR applications due to its potential to guide and monitor minimally invasive procedures and its compatibility with existing clinical equipment and workflow.

5. Conclusion

This work demonstrated the feasibility of using an interstitial source to provide sufficient local fluence in generating reliable PA images that are acquired with an external US array. Multi-wavelength PA imaging was demonstrated on nanoparticle targets in ex-vivo tissue and in tissue-mimicking phantoms. Similar imaging techniques could be used in clinical procedures to provide real-time feedback during PA image-guided biopsies or thermal therapy. As demonstrated by the results of this feasibility study, the clinical role of PA imaging in the future can be further expanded by implementing local, interstitial irradiation for characterizing deeper tissues using conventional clinical US systems.

Conflict of Interest Statement

The authors declare that there are no conflicts of interest.

Acknowledgements

References

[1] Cleary K, Peters TM. Image-guided interventions: technology review and clinical applications. Annual Review of Biomedical Engineering 2010;12:119–42.

[2] Bouchard R, Sahin O, Emelianov S. Ultrasound-guided photoacoustic imaging: current state and future development. Ultrasonics, Ferroelectrics and Frequency Control. IEEE Transactions on 2014;61(3):450–66.

[3] Karabutov AA, Podymova NB, Letokhov VS. Time-resolved laser optoacoustic tomography of inhomogeneous media 1996.

[4] Laser Institute of America, ANSI Z136.1: American National Standard for Safe Use of Lasers, Tech. rep., American National Standards Institute, Laser Institute of America, Orlando, FL (2007).

[5] Homan K, Kim S, Chen Y-S, Wang B, Mallidi S, Emelianov S. Prospects of molecular photoacoustic imaging at 1064 nm wavelength. Optics letters 2010;35(15):2663–5.

[6] Simpson CR, Kohl M, Essenpreis M, Cope M. Near-infrared optical properties of ex vivo human skin and subcutaneous tissues measured using the Monte Carlo inversion technique. Physics in Medicine and Biology 1998;43:2465–78.

[7] Su JL, Bouchard RR, Karpiouk AB, Hazle JD, Emelianov SY. Photoacoustic imaging of prostate brachytherapy seeds. Biomedical Optics Express 2011;2(8):2243–54.

[8] Mitcham T, Homan K, Frey W, Chen Y-S, Emelianov S, Hazle J, Bouchard R. Modulation of photoacoustic signal generation from metallic surfaces. Journal of biomedical optics 2013;18(5). 056008–056008.

[9] Yuan Y, Yang S, Xing D. Preclinical photoacoustic imaging endoscope based on acousto-optic coaxial system using ring transducer array. Optics Letters 2010;35:2266–8.

[10] Sheaff C, Lau N, Patel H, Huang SW, Ashkenazi S. Photoacoustic imaging endoscope. In: Annual International Conference of the IEEE Engineering in Medicine and Biology Society 2009. 2009. p. 1983–6.

[11] Yang J-M, Favazza C, Chen R, Yao J, Cai X, Maslov K, Zhou Q, Shung KK, Wang LV. Simultaneous functional photoacoustic and ultrasonic endoscopy of internal organs in vivo. Nature Medicine 2012;18:1297–302.

[12] Karpiouk AB, Wang B, Emelianov SY. Development of a catheter for combined intravascular ultrasound and photoacoustic imaging. Review of Scientific Instruments 2010;81(1):014901.

[13] Jansen K, Van Der Steen AF, Springeling G, Van Beusekom HM, Oosterhuis JW, Van Soest G. Intravascular photoacoustic imaging of human coronary atherosclerosis. In: SPIE BiOS, International Society for Optics and Photonics; 2011. 789904–789904.

[14] Mitcham T, Marques T, Chatterjee D, Krishnan S, Pugh T, Bouchard R. Transrectal photoacoustic-ultrasonic imaging enhancement through interstitial irradiation and targeted nanoparticles. In: Proceedings of the 2013 IEEE Ultrasonics Symposium; 2013.

[15] Yamamoto S, Nishida T, Kato M, Inoue T, Hayashi Y, Kondo J, Akasaka T, Yamada T, Shinzaki S, Iijima H, Tsujii M, Takehara T. Evaluation of endoscopic ultrasound image quality is necessary in endosonographic assessment of early gastric cancer invasion depth. Gastroenterology Research and Practice 2012.

[16] Gazelle GS, Haaga JR, Rowland DY. Effect of needle gauge, level of anticoagulation, and target organ on bleeding associated with aspiration biopsy. work in progress. Radiology 1992;183(2):509–13.

[17] Cook JR, Bouchard RR, Emelianov SY. Tissue-mimicking phantoms for photoacoustic and ultrasonic imaging. Biomedical optics express 2011;2(11):3193–206.

[18] Dahl JJ, Pinton GF, Palmeri ML, Agrawal V, Nightingale KR, Trahey GE. A parallel tracking method for acoustic radiation force impulse imaging. Ultrasonics, Ferroelectrics and Frequency Control. IEEE Transactions on 2007;54(2):301–12.

[19] Bouchard RR, Dahl JJ, Hsu SJ, Palmeri ML, Trahey GE. Image quality, tissue heating, and frame rate trade-offs in acoustic radiation force impulse imaging. Ultrasonics, Ferroelectrics and Frequency Control. IEEE Transactions on 2009;56(1):63–76.

[20] S. Prahl, Optical properties spectra, accessed: 2014-07-01 (2001). URL http://omlc.org/spectra/.

[21] Lediju Bell MA, Kuo N, Song DY, Boctor EM. Short-lag spatial coherence beamforming of photoacoustic images for enhanced visualization of prostate brachytherapy seeds. Biomedical optics express 2013;4(10):1964–77.

[22] Anderson RR, Parrish JA. The optics of human skin. Journal of Investigative Dermatology 1981;77(1):13–9.

[23] Dawson J, Barker D, Ellis D, Cotterill J, Grassam E, Fisher G, Feather J. A theoretical and experimental study of light absorption and scattering by in vivo skin. Physics in medicine and biology 1980;25(4):695.

[24] Lindner U, Weersink RA, Haider MA, Gertner MR, Davidson SRH, Atri M, Wilson BC, Fenster A, Trachtenberg J. Image guided photothermal focal therapy for localized prostate cancer: phase i trial. The Journal of urology 2009;182(4):1371–7.

[25] Nanospectra Biosciences Inc., Pilot study of AuroLase therapy in refractory and/or recurrent tumors of the head and neck, Tech. Rep. April 2008, Baylor College of Medicine, Houston, TX (2014).

[26] Garcea G, Lloyd T, Aylott C, Maddern G, Berry DP. The emergent role of focal liver ablation techniques in the treatment of primary and secondary liver tumours. European Journal of Cancer 2003;39(15):2150–64.

[27] Zhang HF, Maslov K, Sivaramakrishnan M, Stoica G, Wang LV. Imaging of hemoglobin oxygen saturation variations in single vessels in vivo using photoacoustic microscopy. Applied Physics Letters 2007;90(5):053901.

[28] Welch AJ, van Gemert MJ. Optical-Thermal Response of Laser-Irradiated Tissue. Springer; 2011.

[29] Shah J, Park S, Aglyamov S, Larson T, Ma L, Sokolov K, Johnston K, Milner T, Emelianov SY. Photoacoustic imaging and temperature measurement for photothermal cancer therapy. Journal of Biomedical Optics 2008;13(3):034024.

[30] Lee HJ, Liu Y, Zhao J, Zhou M, Bouchard RR, Mitcham T, Wallace M, Stafford RJ, Li C, Gupta S, Melancon MP. In vitro and in vivo mapping of drug release after laser ablation thermal therapy with doxorubicin-loaded hollow gold nanoshells using fluorescence and photoacoustic imaging. Journal of Controlled Release Society 2013;172(1):152–8.

[31] Dana N, Di Biase L, Natale A, Emelianov S, Bouchard R. In vitro photoacoustic visualization of myocardial ablation lesions. Heart Rhythm 2014;11(1):150–7.

[32] Mallidi S, Luke GP, Emelianov S. Photoacoustic imaging in cancer detection, diagnosis, and treatment guidance. Trends in Biotechnology 2011;29(5):213–21.

Trevor Mitcham received his BS degree is Bioengineering at Rice University in 2012. He is currently a graduate student in Medical Physics at the University of Texas at Houston and the University of Texas MD Anderson Cancer Center Graduate School of Biomedical Sciences in Houston, Texas. His research interests include photoacoustic imaging for diagnostics and therapy guidance.

Marites Melancon is an Assistant Professor in the Department of Interventional Radiology at The University of Texas, M.D. Anderson Cancer Center. She earned her BS degree in chemistry from the University of San Carlos (Cebu, Philippines) and her MS degree in chemistry at Ateneo de Manila University (Manila, Philippines). She received her PhD degree in biomedical science at The University of Texas- Health Science Center at Houston in 2007. Research in Melancon laboratory us primarily focused on the development of therapeutic and diagnostic agents for image-guided interventions.

Katherine Dextraze is currently pursuing her Ph.D. in Medical Physics under the supervision of Dr. Richard R. Bouchard. Her research interests include photoacoustic imaging and image guidance for minimally invasive procedures. She received her B.S. degree in 2011 in Nuclear and Radiological Engineering at the Georgia Institute of Technology in Atlanta, GA. She was granted a specialized M.S. degree in 2013 in Medical Physics from the University of Texas at Houston and the University of Texas MD Anderson Cancer Center Graduate School of Biomedical Sciences in Houston, Texas.
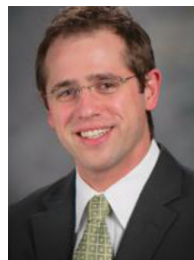
Richard Bouchard received his B.S. degree in biomedical and electrical engineering and cultural anthropology from Duke University in 2004 and received his Ph.D. degree in biomedical engineering from Duke University in 2010. He completed a postdoctoral fellowship in the Ultrasound Imaging and Therapeutics Research Laboratory at the University of Texas at Austin in 2012. Dr. Bouchard is currently an Assistant Professor in the Department of Imaging Physics at the University of Texas MD Anderson Cancer Center. His research interests include preclinical and clinical photoacoustic-ultrasonic imaging and ultrasound-based elasticity imaging.

Houra Taghavi received her B.S. degree in electrical engineering from Azad University, Iran and M.S. degree in Biomedical engineering at Texas A&M University in 2013. She is currently a researcher at University of Texas MD Anderson Cancer Center. Her Research interests include integrated ultrasound and photoacoustic imaging and nanoparticle contrast agents in photoacoustic.